Journal of The
Electrochemical Society

Activity and Durability of Pt/Ir Catalysts for Oxygen Reduction as a Function of Different Platinum Shells

To cite this article: D. Kaplan *et al* 2024 *J. Electrochem. Soc.* **171** 084501

View the article online for updates and enhancements.

You may also like

- Platinum-Iridium Alloys as Oxygen Reduction Electrocatalysts for Polymer Electrolyte Fuel Cells
Tsutomu Ioroi and Kazuaki Yasuda
- Design of Ir/Pt dual electrocatalysts loaded on exfoliated acetylene black for Li air battery application
Lihang Zhou, Koichi Higashimine, Rajashekar Badam et al.
- Electrodeposition and Characterization of Thin-Film Platinum-Iridium Alloys for Biological Interfaces
Artin Petrossians, John J. Whalen, James D. Weiland et al.

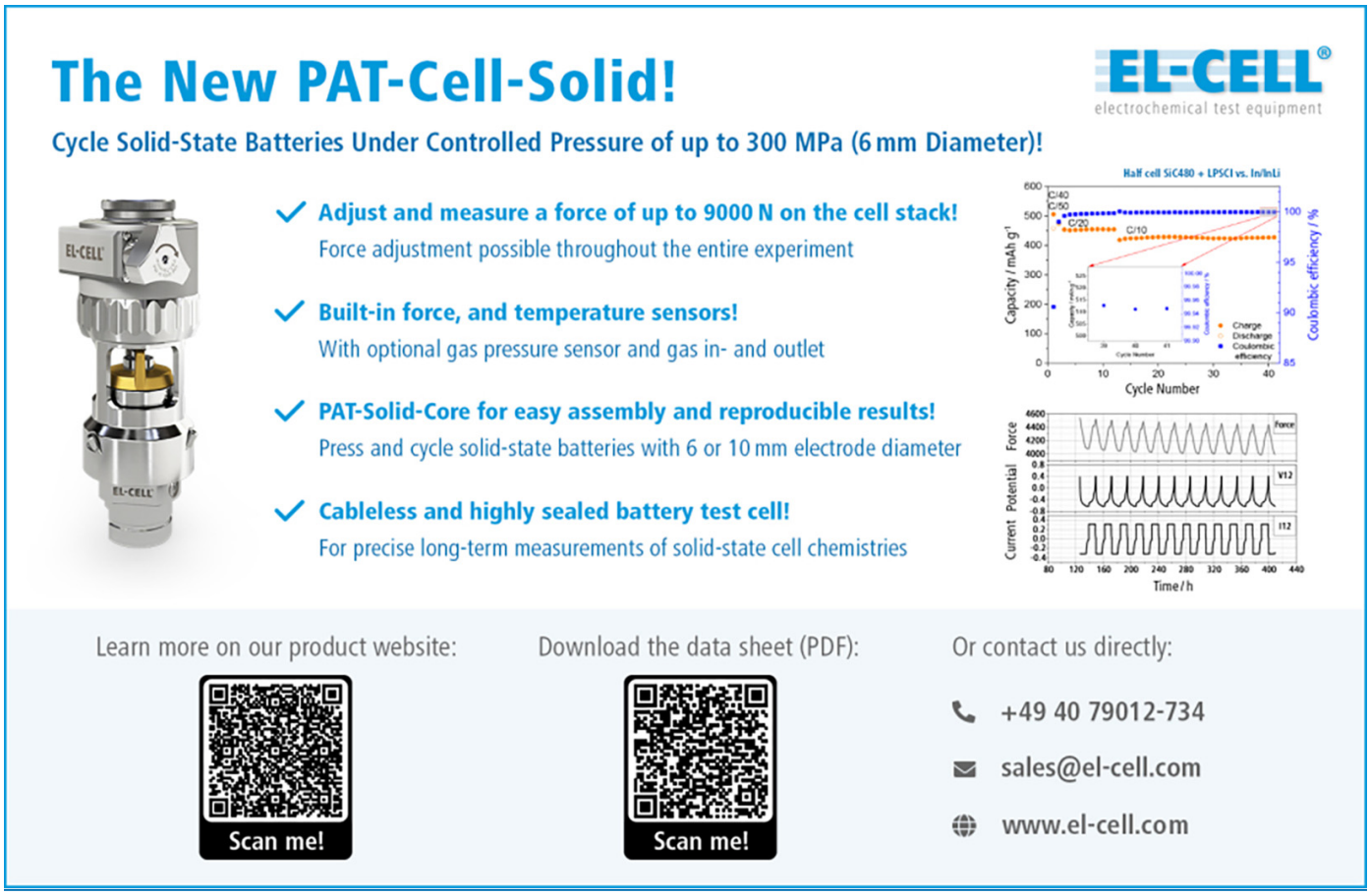

Journal of The Electrochemical Society, 2024 **171** 084501

Activity and Durability of Pt/Ir Catalysts for Oxygen Reduction as a Function of Different Platinum Shells

D. Kaplan,[1,2,z] P. Tereshchuk,[3] S. Sisorov,[1] I. Popov,[4] S. Remennik,[4] L. Burstein,[5] M. Shviro,[6,*,a] A. Natan,[3,z] and E. Peled[1,,z]**

[1]*School of Chemistry, Faculty of Exact Sciences, Tel Aviv University, Tel Aviv, 69978, Israel*
[2]*Nuclear Research Center - Negev, Beer-Sheva, 84190, Israel*
[3]*Department of Physical Electronics, Tel Aviv University, Tel Aviv, 69978, Israel*
[4]*The Hebrew University Center for Nanoscience and Nanotechnology, The Hebrew University of Jerusalem, Jerusalem, 91904, Israel*
[5]*Wolfson Applied Materials Research Center, Tel Aviv University, Tel Aviv, 69978, Israel*
[6]*Institute of Energy and Climate Research, IEK-14, Forschungszentrum Jülich, Jülich, 52428, Germany*

We performed a systematic experimental and theoretical analysis of the oxygen reduction reaction (ORR) activity and durability of Pt/Ir catalysts featuring different platinum shells. Four Pt/Ir catalysts with different platinum monolayers (ML) on an iridium core were synthesized. The nanostructure and composition of the catalysts were studied using scanning transmission electron microscopy with energy–dispersive X–ray spectroscopy, X–ray photoelectron spectroscopy, and scanning electron microscopy with energy–dispersive X–ray spectroscopy. ORR activity and catalyst durability were studied using cyclic voltammetry with rotating disk electrode. Density functional theory calculations were performed to estimate the ORR activity of Pt(111) and nML Pt/Ir(111) surfaces (n = 0, 1, 2). Although the specific ORR activities of the synthesized Pt/Ir catalysts were lower or comparable to those of 50%Pt/C, the mass activities were higher due to the enhanced utilization of platinum. Accelerated stress tests (ASTs) revealed that the durability of 1 ML Pt/Ir surpassed that of the other studied catalysts. The factors influencing the trends in specific and mass activities, durability, and the feasibility of implementing a Pt/Ir system in practical proton exchange membrane fuel cells (PEMFCs) are discussed.
 [DOI: 10.1149/1945-7111/ad6711]

Manuscript submitted March 29, 2024; revised manuscript received June 28, 2024. Published August 5, 2024.

Supplementary material for this article is available online

With the potential for higher efficiency, scalability, flexibility, and zero pollution, PEMFCs are being viewed as a promising power source for vehicular, portable, and stationary applications.[1,2] Both academia and industry have carried out extensive research and development related to PEMFC over the last 30 years. However, despite significant progress, there are still major obstacles to widespread commercialization, such as performance, durability, and cost.[3]

Platinum-based catalysts used in the cathode of PEMFCs have a slow ORR kinetics resulting in overpotentials of 400 mV. This limits the efficiency, power, and energy densities of PEMFCs, and necessitates high platinum-group metals (PGMs) loading on the cathode. Moreover, PGM durability issues require higher PGM loadings to meet the end-of-life performance goals of PEMFC stacks. The US Department of Energy (DOE) has set a target of 0.1 mg_{PGM} cm^{-2} for PEMFC PGM loading in light-duty vehicles (LDVs) by 2025, with a durability of 8000 h.[4] In recent years, the DOE has made significant efforts to promote the use of PEMFC in heavy-duty vehicles (HDVs). This application necessitates significantly greater durability than LDVs, albeit with some compromise in PGM loading. By 2030, the DOE's interim goal for PGM loading in PEMFC cathodes for HDV is 0.3 mg_{PGM} cm^{-2} with a durability of 25000 h. The ultimate goal is a PGM loading of 0.25 mg_{PGM} cm^{-2} with a 30000 h durability.[5,6] Currently, the PGM loadings are 0.2–0.4 mg_{Pt} cm^{-2}[7,8] in LDVs and ∼0.4 mg_{Pt} cm^{-2} in HDVs.[5] These high loadings have an adverse effect on the cost of PEMFCs.

Different strategies and progress to reduce platinum loading in the catalysts were summarized by Debe,[9] Gasteiger et al.,[10,11] Zhang,[12] Schmidt et al.,[13] Stamenkovic et al.,[14] Shao et al.,[15] Banham et al.[16] and Chang.[17] Among these strategies is the use of a core–shell structure with a core that contains little or no platinum and a shell that is mostly or entirely made of platinum.[18–22] Given that electrocatalysis occurs only on the surface of the catalyst, this represents a rational approach to optimize the utilization of platinum atoms. Other potential benefits for ORR catalysis include changes in d-orbital vacancies and Pt–Pt bond distances, which may favorably affect ORR specific activity.[23] Despite extensive research and promising results in ex situ RDE experiments, their transition to commercial fuel cells has not been realized.[24,25]

In one of the well-known studies, Adzic et al.[26] demonstrated that, in comparison to a Pt(111) surface, a platinum monolayer on Pd (111) exhibits a mildly compressive strain, leading to a slightly decreased d-band center (ε_d), and a slightly weaker oxygen binding. Consequently, this results in an approximately 30% increase in ORR specific activity. This finding opened up the possibility of using nanoparticles with a Pd_{core}-Pt_{shell} structure as catalysts for ORR.[18,25,27] However, it was also found that, during potential cycling, the Pt-on-Pd structure experiences transient dissolution of platinum and palladium[28] and undergoes structural collapse.[29]

A possible approach to address the issues of platinum dissolution and structural collapse during potential cycling is to incorporate a stabilizing component into the catalyst structure. This additional component can either be alloyed with platinum[30,31] or used as a core for a platinum shell.[32–35]

Iridium holds promise as a stabilizing component for platinum shells. According to DFT calculations by Le Page et al., the Pt-Ir bond exhibits greater strength than both Pt-Pt and Ir-Ir bonds.[36] Greeley et al.[37] and Balbuena et al.[38] have predicted the stabilization of platinum on iridium substrate. There are also several experimental studies demonstrating improved durability of the Pt-Ir system (PtIr alloy and Ir_{core}-Pt_{shell}) in comparison to pure platinum.[30,31,39–45] However, this stabilization effect may be accompanied by a reduction in the ORR specific activity. It was found that a platinum monolayer on Ir(111) surface undergoes a significant compressive

*Electrochemical Society Member.
**Electrochemical Society Fellow.
[a]Present address: Chemistry and Nanoscience Center, National Renewable Energy Laboratory (NREL), Golden, Colorado 80401, USA.
[z]E-mail: dimakapl@tauex.tau.ac.il; peled@tauex.tau.ac.il; amirnatan@post.tau.ac.il

strain, resulting in a lowered d-band center (ε_d) and suboptimal oxygen binding. Consequently, the catalytic activity of a platinum monolayer on Ir(111) is lower compared to that on a Pt(111) surface.[26]

A study by Adzic et al. on the Pt_{XML}/Ru/C catalysts (ML=monolayer, X = 1, 2, 3) revealed that a Pt_{1ML}/Ru/C catalyst demonstrated a lower specific ORR activity compared to 20%Pt/C.[46] This result was explained by the negative influence of ruthenium on the O–O bond-scission activity of platinum. In contrast, Pt_{2ML}/Ru/C and Pt_{3ML}/Ru/C catalysts exhibited a higher specific ORR activity than 20%Pt/C. These findings clearly indicate that the negative effect of the core metal on ORR can be mitigated by incorporating multiple layers of platinum in the shell.

Guided by these findings, we performed a systematic study on the effect of different platinum shells in the Pt/Ir system on the ORR catalytic activity and durability. Carbon-supported iridium nanoparticles served as the core material. Utilizing electroless deposition with $NaBH_4$ as the reducing agent, we deposited platinum in quantities equivalent to ¼ML, ½ML, 1ML, and 2ML onto the iridium nanoparticles.[45] In comparison to the synthesis of core–shell nanoparticles using under-potential deposition coupled with galvanic displacement[25] or the polyol method[47] and its derivatives,[27] the strong reducing nature of $NaBH_4$ limits the ability to fine-tuning the resulting platinum morphology. Nonetheless, it proves to be a rapid, straightforward, cost-effective, and relatively eco-friendly method, crucial factors for large-scale industrial production. To enhance the controllability of platinum deposition to some extent, a step-by-step process was employed, depositing an amount equivalent to ¼ML of platinum on iridium nanoparticles during each deposition step.[45]

To determine their composition and nanostructure, the synthesized catalysts were characterized by SEM-EDS, TEM, STEM-EDS and XPS. The electrochemically active surface area (ECSA), ORR activities and catalyst durability were assessed using CV with RDE technique, with comparisons made to the characteristics of 40%Ir/XC72 and 50%Pt/C. In elucidating the impact of different platinum shells on the ORR activity, we employed DFT simulations to estimate the ORR activity on Pt(111) and nML Pt/Ir(111) surfaces (n = 0, 1, 2). To achieve this, we conducted DFT simulations to investigate the adsorption of platinum atoms on the Ir(111) surface and their influence on the O and OH binding energies on the resulting surfaces. Additionally, climbing image nudged elastic band (CI-NEB) calculations were conducted to determine the activation energies for O_2 dissociation and OH formation. We then followed the procedure proposed by Nørksov et al. to estimate the ORR activity.[48] The combined experimental and computational work provides an extensive insight into how varying platinum shells on iridium influence both the ORR activity and durability of Pt/Ir catalysts.

Experimental Methods

Catalysts synthesis.—The catalysts were synthesized by electroless deposition of platinum on commercial 40 wt% Ir/XC72 (Premetek, particle size 3.6 nm according to XRD[44,45]), utilizing $NaBH_4$ as the reducing agent. To enhance control over platinum deposition, a successive step-by-step deposition process of platinum was implemented.[45] Briefly, in each deposition step, an amount of platinum equivalent to ¼ML on iridium nanoparticles was deposited by adding the appropriate quantity of platinum precursor (a solution of 0.4 M HCl + $PtCl_4$), ammonium hydroxide solution, and reducing agent. These steps were repeated as needed to produce Pt/Ir particles with platinum amounts equivalent to ¼ML, ½ML, 1 ML, and 2 ML. The catalysts will be designated as follows: ¼ML Pt/Ir, ½ML Pt/Ir, 1 ML Pt/Ir, and 2 ML Pt/Ir.

The obtained powder was washed with distilled water until no chloride ions could be detected,[49] followed by drying through liquid evaporation. In the final synthesis step, the powder was subjected to a hot treatment with 0.5 M H_2SO_4 at 80 °C for eight hours to dissolve unstable moieties from the nanoparticle surface, followed by a subsequent wash with distilled water.

Electrochemical characterization.—For electrochemical studies, a 5 mm–diameter glassy–carbon RDE (Pine Instruments, USA, $A_{geo} = 0.196$ cm^2) polished to a mirror finish with a 0.05 μm Al_2O_3 particle suspension on a moistened polishing Micro–Cloth (both from Buehler) was employed. It was attached to an interchangeable RDE shaft connected to an electrode rotator (MSRX electrode rotator, Pine Instruments, USA). A Pt–wire served as the counter electrode, and an Ag/AgCl/3 M KCl reference electrode (Metrohm) within a Luggin-capillary compartment were utilized in a custom-made three-compartment electrochemical cell. A Biologic SP300 potentiostat was used to obtain CVs, ORR I-V polarization curves, and high-frequency resistance (HFR) values derived from Nyquist plots, with the latter used for iR drop corrections. All potentials are reported with respect to the reversible–hydrogen–-electrode (RHE) scale and all experiments were performed at room temperature (25 ± 2 °C).

The catalytic ink formulation consisted of 5 mg of catalyst powder, a 5 wt% Nafion solution, XC72, deionized (DI) H_2O and isopropyl alcohol (IPA). The volume of the Nafion solution was adjusted to constitute approximately ∼30% (v/v) of the solids in the inks. The addition of XC72 aimed to enhance ink stability and promote a uniform catalyst coating on the RDE. The solids concentration in the ink was set to ∼0.2%(w/w). The volume of DI H_2O and IPA was adjusted to achieve a catalytic loading of ∼20 μg_{PGM} cm_{geo}^{-2} on the RDE, with the IPA/(IPA+H_2O) ratio set to ∼30%(v/v).[50]

The catalytic ink was subjected to ultrasonic dispersion for 60 min in an ultrasonic bath, with an additional five-minute dispersion using a horn sonicator (Heilscher UP200st). Throughout these sonication processes, the vial containing the ink was cooled by an ice-water bath. Subsequently, 10 μl of the ink was pipetted onto the RDEs. To prevent rapid settling of solids in the ink during the pipetting process, ultrasonication in the ultrasonic bath was applied. The metal loadings on the RDE were ∼20 μg_{PGM} cm_{geo}^{-2}. **Platinum–only** loadings for the different Pt/Ir/XC72 catalysts were 2 μg_{Pt} cm_{geo}^{-2} (¼ML Pt/Ir), 3.4 μg_{Pt} cm_{geo}^{-2} (½ML Pt/Ir), 5.1 μg_{Pt} cm_{geo}^{-2} (1 ML Pt/Ir) and 9.7 μg_{Pt} cm_{geo}^{-2} (2 ML Pt/Ir).

The uniformity of the catalytic film was demonstrated to significantly impact the currents observed in RDE ORR polarization.[51–53] Following an evaluation of various ink droplet drying procedures, it was determined that, under our laboratory conditions, a stationary drying method at room temperature in an IPA environment consistently yielded the most uniform catalytic films.[45,49] Consequently, this drying approach was employed throughout the course of this research.

Before performing electrochemical evaluations of the catalysts, a conditioning procedure was performed to obtain peak ECSA and ORR activity. A typical conditioning procedure for Pt/C catalysts involves repetitive cycling in deaerated electrolyte within a potential range of 0–1.2/1.4 V until a stable voltammogram is attained.[54] Literature reports indicate that cycling bulk iridium electrodes to these upper potentials limits (UPLs) leads to significant irreversible oxidation of iridium.[55–57] Cycling of 40%Ir/XC72 to a UPL of 1.2 V at a scan rate of 20 mV s^{-1} resulted in an irreversible oxidation (Fig. S1a in Supplementary Material (SM)). Some degree of irreversible oxidation occurred during repetitive fast cycling (⩾200 cycles) to a UPL of 900 mV (Fig. S1b in the SM). Given that oxidized iridium cannot adsorb hydrogen through underpotential deposition, and considering that the hydrogen–stripping method was employed for determining ECSAs, such oxidation would result in inaccurate ECSA measurements for Ir-based catalysts. Therefore, considering the presence of iridium on their surface, it was decided to condition 40%Ir/XC72, ¼ML Pt/Ir, ½ML Pt/Ir, and 1 ML Pt/Ir catalysts by cycling to the UPL of 800 mV. As 2 ML Pt/Ir showed no clear indication of iridium on the surface, it was conditioned by cycling to

the UPL of 1200 mV. The same UPL was applied to the commercial 50%Pt/C. The conditioning procedure involved 100 cycles (200 cycles for 40%Ir/C) at a scan rate of 500 mV s^{-1}. The electrolyte was deaerated by bubbling N_2 (99.999%) through it for a minimum of 25 min. N_2 was continuously passed over the quiescent electrolyte during cycling. These conditioning procedures consistently produced stable and reproducible voltammograms.

The ECSAs of the studied catalysts were determined by the standard hydrogen–stripping method.[58] A charge density of 210 $\mu C/cm^2_{Pt}$, commonly employed during hydrogen–stripping for platinum ECSA measurements, was used.[54] It has been reported that the hydrogen–stripping charge density for iridium is 218 $\mu C/cm^2_{Ir.}$[59] For simplicity, and given their small differences, the same charge density value as that used for platinum was employed for iridium, following a similar approach chosen by Gasteiger et al.[60] The working electrodes with 2 ML Pt/Ir and 50%Pt/C catalysts underwent five cycles within a potential range of 0.025–1.2 V at 20 mV s^{-1} in deaerated electrolyte. The ECSA value was determined from the voltammogram of the last cycle, which was also utilized for background measurements. ¼ML Pt/Ir, ½ML Pt/Ir, and 1 ML Pt/Ir catalysts were also cycled five cycles for ECSA measurement, but within a potential range of 0.025–0.8 V to avoid affecting the ECSA value through irreversible oxidation of iridium. Subsequently, for background measurements and better comparison of the Ir/Pt-oxides reduction peaks, the catalysts were cycled within a potential range of 0.025–1.2 V. 40%Ir/XC72 catalyst was cycled within a potential range of 0.025–0.8 V for ECSA measurement. However, cycling for background measurements was limited to 0.9 V to prevent any influence of irreversible oxidation of iridium on ORR activity. Separate 40%Ir/XC72 electrodes, not utilized for ORR and AST measurements, were cycled within a potential range of 0.025–1.2 V for the comparison of Ir/Pt-oxides reduction peaks.

For ORR measurements, the electrolyte was oxygen-saturated by bubbling O_2 (99.999%) through it for a minimum of 25 min. The RDE was rotated at 2500 rpm and cycled within a potential range of 1–0 volts at 20 mV s^{-1} for three times. Continuous O_2 flow over the electrolyte was maintained during cycling. The current at 0.85 V during anodic sweep polarization, following mass transport,[51,54] background,[54] and iR drop[61] corrections, served as an indicator of the ORR activity, $i^{0.85V}$.[62]

AST measurements were performed by cycling the working electrode in deaerated electrolyte for 5000 cycles at 50 mV s^{-1} over the 0.6–0.9 V potential range. This potential range was selected to simulate real-world conditions applicable to the operational life of the PEMFC cathode.[63,64] Continuous N_2 flow over the electrolyte was maintained during cycling. After completing the AST cycles, the ECSA and ORR activity of the catalysts were re-evaluated. The ORR current density after AST was taken as a durability measure of the ORR activity.

All ECSA and ORR activity values presented are the averages of at least three samples, with standard deviations of the results not exceeding 5%.

Physical characterization.—XPS measurements were performed with the use of a 5600 Multi-Technique System (PHI, USA). The samples were irradiated (in ultra-high vacuum, 2.5×10^{-10} torr base pressure) with an Al Kα monochromated source (1486.6 eV) and the emitted electrons were analyzed by a spherical capacitor analyzer with a slit aperture of 0.8 mm. They were analyzed on the surface and after sputter cleaning with the 4 kV Ar^+ ion gun, at a sputter rate of 39 Å min^{-1} on a reference SiO_2/Si sample. Pt4f and Ir4f binding energies were used for measurements of atomic ratios. SEM-EDS measurements were performed with the use of FEI Quanta 200 FEG SEM. The microscope was operated at 20 kV. Oxford–INCA detector and software were employed for EDS measurements, using Pt M and Ir M peaks. EDS and XPS measurements were conducted at ten and four points, respectively, and the results revealed no significant inhomogeneity. The presented results represent the average of these measurements.

TEM imaging was performed with an FEI F20 Philips-Tecnai STEM operated at 200 kV. Samples were prepared by manually pressing the grid (200-mesh grid, EMS) against the sample powder. Particle size distributions were reconstructed by determining the diameter of at least 100 individual particles using ImageJ software,[60] based on TEM images captured at high magnification.

For STEM-EDS elemental mapping, a ThermoFisher probe-corrected STEM Themis Z G3 electron microscope, equipped with a Fishione HAADF STEM detector and ThermoFisher Super-X G2 EDS detector system, was employed. The microscope was operated at 300 kV, and Pt L and Ir L peaks were used during elemental mapping. Samples were prepared by depositing a diluted catalyst suspension droplet on a 400-mesh carbon-coated copper grid.

Computational Methods

We performed total energy calculations using Density Functional Theory (DFT) with the Perdew–Burke–Ernzerhof generalized gradient approximation (PBE-GGA)[65] as the exchange-correlation energy functional. The projected augmented wave (PAW)[66,67] method was employed, and the calculations were performed within the Vienna *Ab initio* Simulation Package (VASP) code.[68,69] For the platinum and iridium bulk and slab surface calculations, we applied a plane wave cut-off energy of 500 eV, and k-point grids of $10 \times 10 \times 10$ and $6 \times 6 \times 1$ for cells, respectively. For structural energy minimization, we set up the maximal atomic forces on each atom as 0.02 eV $Å^{-1}$, and a total energy convergence criterion of 10^{-6} eV was used.

The bulk crystal structure of both platinum and iridium is face-centered cubic (fcc). Our calculated equilibrium lattice constants are 3.968 Å and 3.873 Å for platinum and iridium, respectively. These values align well with theoretical data obtained from the Aflow database[70] and are consistent with both PBE theoretical predictions and experimental findings in the literature.[71–73]

We created slabs of (111) surfaces and (3×3) surface unit cells for platinum and iridium, which correspond to a hexagonal surface

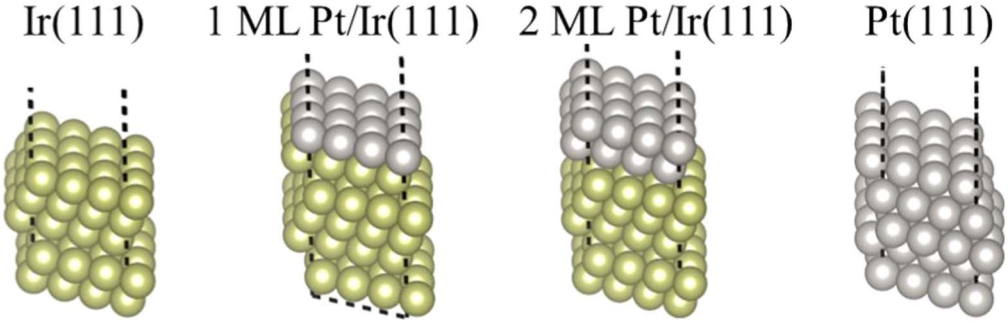

Figure 1. Clean surfaces for nML Pt/Ir(111) ($n = 0$, 1, 2) and Pt(111). Iridium atoms are shown in yellow; platinum atoms are shown in gray.

cell with a lattice constant of 8.42 Å and 8.22 Å, respectively. The slab thickness was set to 5 layers, resulting in 9.08 Å for platinum and 8.88 Å for iridium. In both cases, a vacuum region of 22 Å was employed.

We covered the Ir(111) surface with 1 and 2 ML of platinum atoms, placing them on the positions that reproduce the ABC stacking of the slab. Then we optimized the created structures, freezing the two bottom atomic layers, while the remaining layers were allowed to move. The optimized structures for Ir(111), 1 ML and 2 ML Pt on Ir(111) and Pt(111) are given on Fig. 1.

Modelling of O and OH on nML Pt/Ir(111) (n = 0, 1, 2) and Pt (111) surfaces.—We modeled O and OH species on the surfaces by placing them on the hollow, bridge and top sites over the metal surfaces. During optimization, we allowed all the atoms to relax, except for the two bottom layers which were frozen. We collected all the structures and selected the lowest energy structures.

Binding energies, reaction energies, and activity.—We calculated the binding energies for all cases as:

$$E_b = E^{mol/surf} - E^{surf} - E^{mol} \quad [1]$$

where the first, second, and third terms are the total energies of the molecular species on the surfaces, total energies of the clean surface, and total energies of the molecular species in the gas-phase, respectively.

In order to correctly calculate the activity of our systems, we take into account the effect of water by employing the implicit solvation model of VASPSol[74,75] as implemented in VASP.

For the calculations of the activity, we followed the procedure proposed by Nørskov et al.[48] For that, we calculated the reaction energies ΔE_O and ΔE_{OH} for the following reactions

$$H_2O + * \rightarrow O_* + H_2(\Delta E_O), \quad [2]$$

$$H_2O + * \rightarrow OH_* + 1/2H_2(\Delta E_{OH}). \quad [3]$$

where "*" is the clean surface, and O* and OH* are the adsorbed molecules.

To obtain the respective ΔG s we added the ΔZPE—TΔS corrections to the reaction energies of the systems, where ΔZPE and ΔS represent the changes in zero-point energy and entropy resulting from the reaction, respectively. The ΔZPE—TΔS corrections, taken from,[48] are 0.35 for (*OH + 1/2H_2) and 0.05 for (*O + H_2).

We calculated $\Delta G(U_0)$ as

$$\Delta G_0(U_0) = \Delta E_O - 2eU_0, \quad [4]$$

$$\Delta G1(U_0) = \Delta E_{OH} - \Delta E_O + eU_0, \quad [5]$$

$$\Delta G2(U_0) = -\Delta E_{OH} + eU_0. \quad [6]$$

where $2eU_0 = 2.46$ eV.

While the calculated ΔG s show the intermediate state barriers, there are also significant energy barriers arising from transition states. In the ORR those barriers are typically associated with the O_2 dissociation and the OH formation at the surface. The O_2 dissociation barrier can be estimated from ΔE_O using the universal scaling relationships[48] although deviations from the linear relation may occur. Therefore, we conducted CI-NEB calculations, as implemented in VASP,[76,77] to calculate the activation energy barriers, E_A, for O_2 dissociation and OH formation at the surface by:

$$E_A = E_{TS} - E_{IS}, \quad [7]$$

where E_{TS} and E_{IS} are the energies of the transition and initial states.

Using the obtained results, we calculated the activity (A) as

$$A = -\max\ (\Delta G_0(U_0),\ \Delta G_1(U_0),\ \Delta G_2(U_0),\ E_A(O_2),\quad E_A(OH)). \quad [8]$$

Equation 8 is similar to the expression which is used by Nørskov et al. in[48] for the activity estimation, with some modifications. Firstly, we employ CI-NEB calculations instead of scaling relationships to estimate $E_A(O_2)$. Secondly, we incorporate the CI-NEB-calculated $E_A(OH)$ to the expression, recognizing the significance of the OH formation barrier in influencing the ORR activity.

Results and Discussion

Structure and composition analysis.—Comparison of EDS and XPS analysis of the catalysts is presented in Table I. EDS analyses showed that the weight composition for the synthesizeld catalysts was $Pt_{4\%}/Ir_{38\%}$/XC72 for ¼ML Pt/Ir, $Pt_{8\%}/Ir_{37\%}$/XC72 for ½ML Pt/Ir, $Pt_{13\%}/Ir_{34\%}$/XC72 for 1 ML Pt/Ir and $Pt_{29\%}/Ir_{28\%}$/XC72 for 2 ML Pt/Ir (Table I). **All** synthesized catalysts exhibited different surface and bulk concentrations of platinum. For example, the bulk atomic Pt:Ir ratio (from EDS) for 1 ML Pt/Ir was $Pt_{28}Ir_{72}$ while the surface atomic ratio (from XPS) was $Pt_{59}Ir_{41}$; after one minute of sputtering, the latter decreased to $Pt_{46}Ir_{54}$. These findings indicate that, although iridium is the predominant metal in the synthesized catalysts (according to EDS), this metal is predominant in the core, while the surface becomes increasingly enriched with platinum (from ¼ML Pt/Ir to 2 ML Pt/Ir).

Representative TEM images along with size-distribution histograms (included as insets) of the studied catalysts are presented in Figs. S2a–S2f in the SM. Table I shows the average particle sizes for each catalyst. The average particle size for 50% Pt/C was 3.7 ± 1 nm, in good agreement with the crystallite size measured by XRD, 3.8 ± 0.1 nm.[44] The average particle size for 40%Ir/XC72 was 3.4 ± 0.6 nm, also similar to the crystallite size obtained using XRD analysis, 3.6 ± 0.1 nm.[44] The average particle sizes of the synthesized catalysts are quite similar to 40%Ir/XC72 up to 1 ML Pt/Ir (3.7–3.9 nm), and increasing substantially to 4.4 nm for 2 ML Pt/Ir.

Figures 2a–2d show representative high-resolution STEM-EDS mappings of the Pt/Ir catalysts. A mapping of single nanoparticles can be seen for each catalyst, with platinum colored in red and

Table I. Physical characterization results of the studied catalysts.

Catalyst	Bulk wt% ratio (EDS)	Bulk at% ratio (EDS, metal only)	Surface at% ratio (XPS)	Sub-surface at% ratio (XPS)[a)]	Particle size (TEM, [nm])
50%Pt/C	Pt_{50}	Pt	Pt	Pt	3.7 ± 1
40%Ir/XC72	Ir_{40}	Ir	Ir	Ir	3.4 ± 0.6
¼ML Pt/Ir	Pt_4Ir_{38}	$Pt_{10}Ir_{90}$	$Pt_{22}Ir_{78}$	$Pt_{16}Ir_{84}$	3.8 ± 0.8
½ML Pt/Ir	Pt_8Ir_{37}	$Pt_{18}Ir_{82}$	$Pt_{42}Ir_{58}$	$Pt_{32}Ir_{68}$	3.7 ± 0.8
1 ML Pt/Ir	$Pt_{13}Ir_{34}$	$Pt_{28}Ir_{72}$	$Pt_{59}Ir_{41}$	$Pt_{46}Ir_{54}$	3.9 ± 0.7
2 ML Pt/Ir	$Pt_{29}Ir_{28}$	$Pt_{51}Ir_{49}$	$Pt_{85}Ir_{15}$	$Pt_{76}Ir_{24}$	4.4 ± 1

A) following 1 min sputtering time.

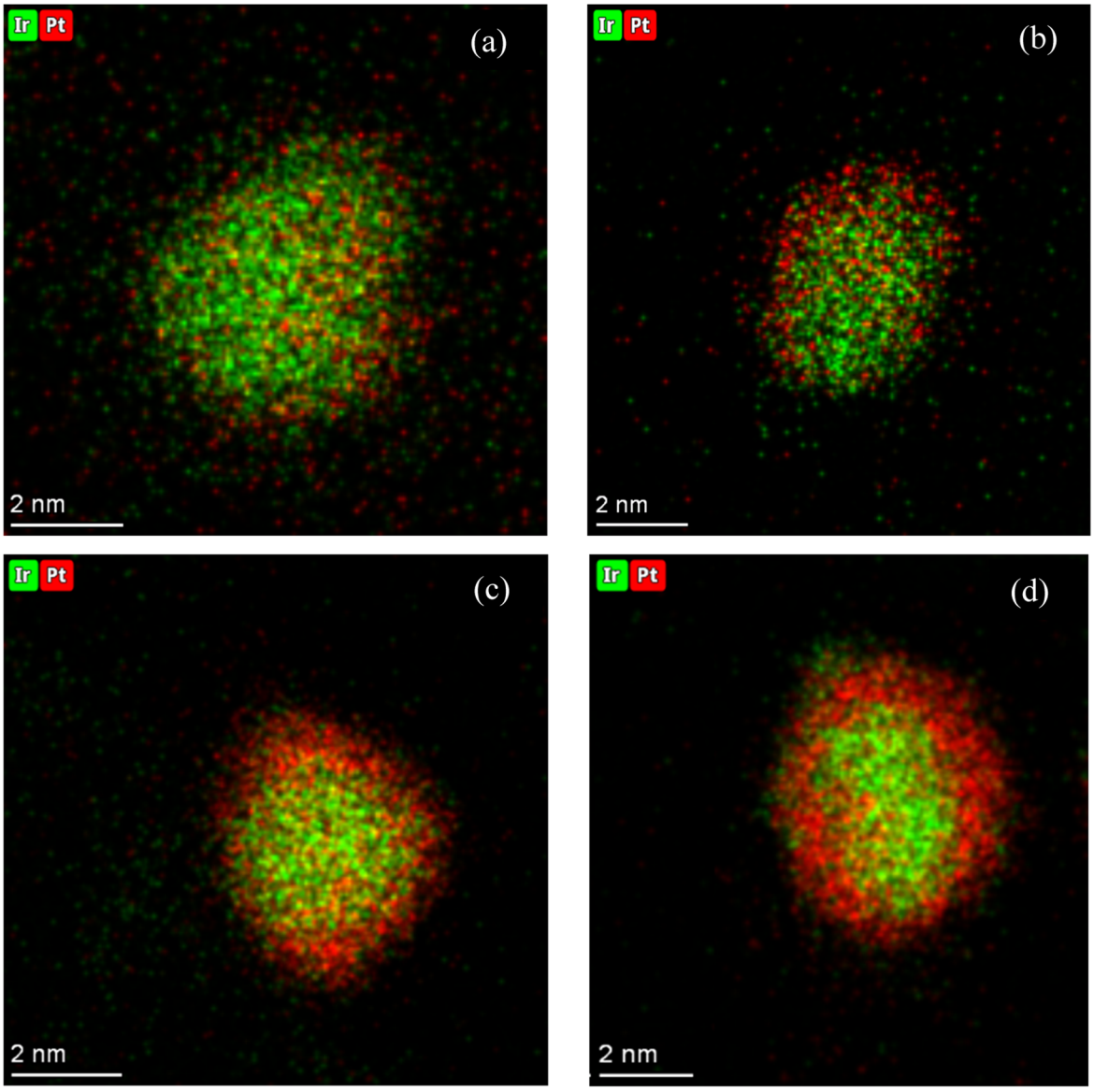

Figure 2. STEM-EDS elemental mapping of the synthesized catalysts. Platinum is marked with red and iridium is marked with green. (a) −¼ML Pt/Ir, (b) −½ML Pt/Ir, (c) −1 ML Pt/Ir, (d) −2 ML Pt/Ir.

iridium in green. Across all Pt/Ir catalysts examined, both iridium and platinum are consistently present in all particles. It can be clearly seen that platinum was deposited on the surface of iridium nanoparticles without creating separate nanoparticles or nano-islands on the carbon support or on the iridium nanoparticles. The mapping of a nanoparticle of ¼ML Pt/Ir (Fig. 2a) shows atomic clusters and probably single atoms of platinum on the iridium nanoparticle. These atomic clusters become more abundant in the mapping of ½ML Pt/Ir (Fig. 2b). The mapping of 1 ML Pt/Ir shows a shell of platinum, albeit not a uniform one, around the iridium nanoparticle (Fig. 2c). The thickness of the platinum shell increases in 2 ML Pt/Ir (Fig. 2d), appearing to cover the iridium core entirely.

Unlike TEM, which examines only few nanoparticles, a CV response originates from the entire sample on the working electrode, leading to a more representative result. Therefore, CV can be a powerful supporting tool in the analysis of surface composition of PGM nanoparticles.

The voltammograms of the 50%Pt/C, 40%Ir/XC72, and Pt/Ir catalysts are shown in Fig. 3. The voltammogram of the 50%Pt/C catalyst (Fig. 3a) exhibits typical platinum features: hydrogen desorption from the 110 and 100 planes during the anodic sweep, occurring at approximately 0.1 V and 0.2 V, respectively, and the reduction of platinum oxide during the cathodic sweep, occurring at approximately 0.75 V. The onset of platinum oxidation is observed at ∼0.75 V during the anodic sweep.[58,78]

The voltammogram of the 40%Ir/XC72 catalyst (Fig. 3b) is consistent with voltammograms of iridium previously published in the literature.[55,57] The hydrogen region includes two hydrogen desorption peaks in the anodic sweep: a broad peak at approximately 0.05–0.1 V that originates from desorption of hydrogen from 111 and 110 planes, and another one at approximately 0.2 V arising from desorption of hydrogen from 100 plane.[79] The more oxyphilic nature of iridium, in comparison to platinum, results in significantly different electrochemical manifestation of the oxidation and reduction processes in their voltammograms. The onset of iridium oxidation occurs at a much lower potential than in the case of platinum; ∼0.35 V vs ∼0.75 V. Additionally, the iridium oxide reduction peak during the cathodic sweep is also at a lower potential compared to platinum oxide; ∼0.5 V vs ∼0.75 V. The distinguishable variations in the voltammograms of platinum and iridium enable a correlation between the voltammograms of Pt/Ir catalysts and their STEM-EDS mappings.

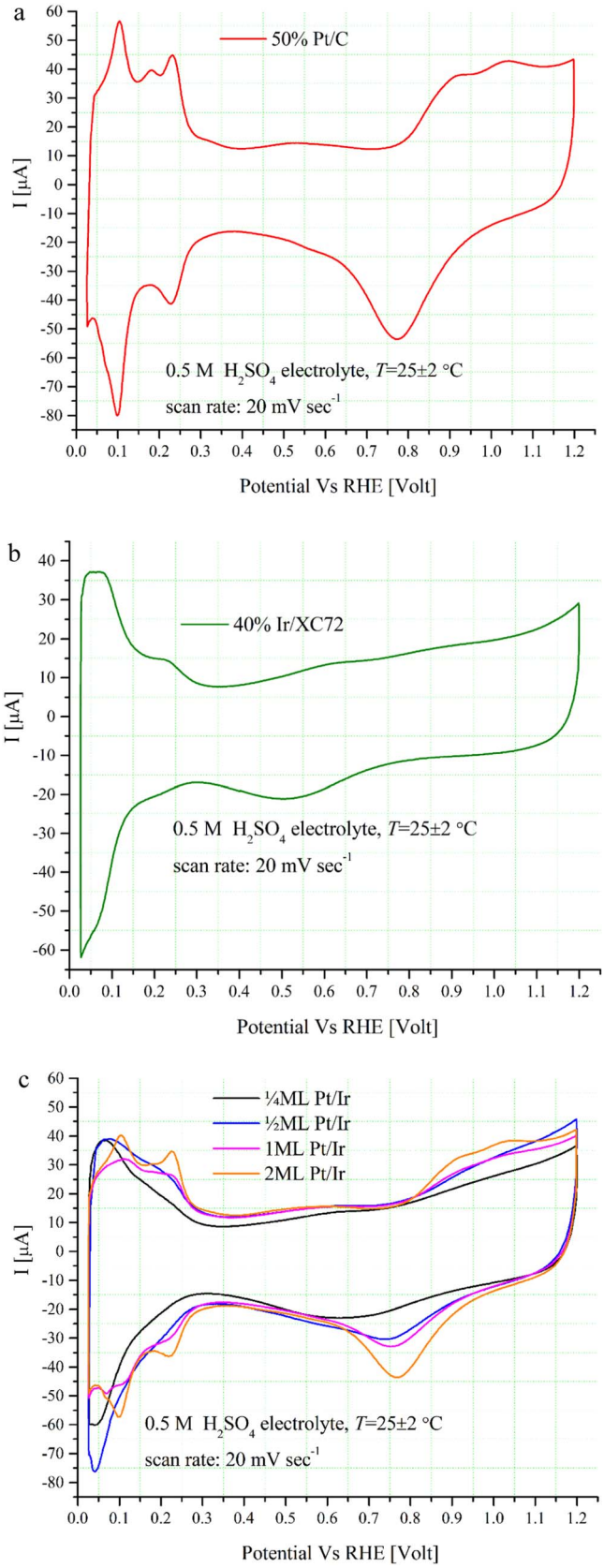

Figure 3. Voltammograms of the studied catalysts in deaerated 0.5 M H_2SO_4, (a) 50%Pt/C, (b) 40%Ir/XC72, (c) Pt/Ir catalysts.

The hydrogen-desorption region observed on the voltammogram of ¼ML Pt/Ir (Fig. 3c, black line) exhibits some similarity to that of 40%Ir/XC72 (Fig. 3b). While there is a broad peak indicative of hydrogen desorption from the 111 and 110 planes, the peak associated with the 100 plane is suppressed. As the platinum content increases on the catalyst surfaces, the hydrogen-desorption region undergoes a transition towards a profile more akin to platinum. In the case of 1 ML Pt/Ir, distinct peaks corresponding to hydrogen desorption from platinum crystal planes 110 and 100 become apparent. However, the overall profile of the hydrogen region suggests the presence of iridium on the surface. In contrast, for 2 ML Pt/Ir (Fig. 3c, orange line), the hydrogen region closely resembles platinum; the hydrogen desorption peaks are sharp and align with those observed for hydrogen desorption from the 110 and 100 planes in 50%Pt/C (Fig. 3a) with no clear indication of iridium presence.

The oxide-reduction peak of ¼ML Pt/Ir exhibits similarities to that of 40%Ir/XC72, albeit with a broader profile and a slight shift towards higher potentials. This suggests a predominance of iridium with some platinum present on the surface of ¼ML Pt/Ir. As the platinum content increases in the Pt/Ir catalysts, the oxide-reduction peak undergoes a noticeable change in its shape. Comparing the voltammograms of ½ML Pt/Ir (Fig. 3c, blue line) and 1 ML Pt/Ir (Fig. 3c, purple line) to that of ¼ML Pt/Ir, the peak sharpens and shifts towards more positive potentials. This shift is more pronounced in the case of 1 ML Pt/Ir than for ½ML Pt/Ir, indicating a lower iridium content and a higher platinum content on the surface of 1 ML Pt/Ir compared to ½ML Pt/Ir. The shape of the oxide-reduction peak for 2 ML Pt/Ir (Fig. 3c, orange line) closely resembles that of 50%Pt/C and does not display any visible indication of iridium on the surface of 2 ML Pt/Ir.

In summary, the voltammograms of the Pt/Ir catalysts align well with the progressively growing platinum shell observed in their STEM-EDS mappings (Fig. 2). There is also a good correlation with the XPS-determined surface composition (Table I), considering that the XPS signal integrates the signals from several top atomic layers.[80]

The combine analysis of Pt/Ir catalysts by STEM-EDS mapping and CV leads to the conclusion that platinum was deposited on the iridium cores without creating platinum nanoparticles. Nearly complete and complete platinum shells were formed in the case of 1 ML Pt/Ir and 2 ML Pt/Ir, respectively. These results demonstrate that by finely tuning a $NaBH_4$-based synthesis, it is indeed possible to produce a Pt-on-Ir structure with a Pt-shell, despite the strong reducing nature of $NaBH_4$. However, it is evident that the resulting platinum shells exhibit non-uniformity.

ECSA and experimentally measured ORR catalytic activity.— The ECSA measurements of the examined catalysts were performed using hydrogen stripping. The obtained values were 49 $m^2\ g^{-1}{}_{Pt}$ for 50%Pt/C, 34 $m^2\ g^{-1}{}_{Ir}$ for 40%Ir/XC72, 35 $m^2\ g^{-1}{}_{PtIr}$ for ¼ML Pt/Ir, 33 $m^2\ g^{-1}{}_{PtIr}$ for ½ML Pt/Ir and 32 $m^2\ g^{-1}{}_{PtIr}$ for 1 ML Pt/Ir and 2 ML Pt/Ir (Table II).

Figure 4 shows the ORR polarization curves of the catalysts, normalized to the geometric area of the working electrode. The measured limiting-current density and ORR specific activity at 0.9 V for the 50%Pt/C catalyst, ~6 mA $cm^{-2}{}_{geo}$ and 0.59 A $m^{-2}{}_{Pt}$ respectively, are in line with results reported for high-surface-area Pt/C catalysts[50,51,81] and single-crystal-platinum electrodes[82] under similar experimental conditions.

When comparing the electrocatalytic activity of catalysts, it is best to normalize their ORR current, $i^{0.85V}$, by their platinum or PGM weight (mass activity, $j_{MA}^{0.85V}$) or by ECSA (specific activity, $j_k^{0.85V}$).[51] The ¼ML Pt/Ir catalyst exhibited a slightly higher ORR mass activity than the 50%Pt/C catalyst: 132 A $g^{-1}{}_{Pt}$ vs 124 A $g^{-1}{}_{Pt}$ respectively. However, the other Pt/Ir catalysts demonstrated significantly higher mass activities, ranging from 43% to 24% higher than those of the commercial catalyst (Table II): 178 A $g^{-1}{}_{Pt}$ for ½ML Pt/Ir, 154 A $g^{-1}{}_{Pt}$ for 1 ML Pt/Ir and 155 A $g^{-1}{}_{Pt}$ for 2 ML Pt/Ir. In contrast, the mass activity of the 40%Ir/XC72 catalyst was

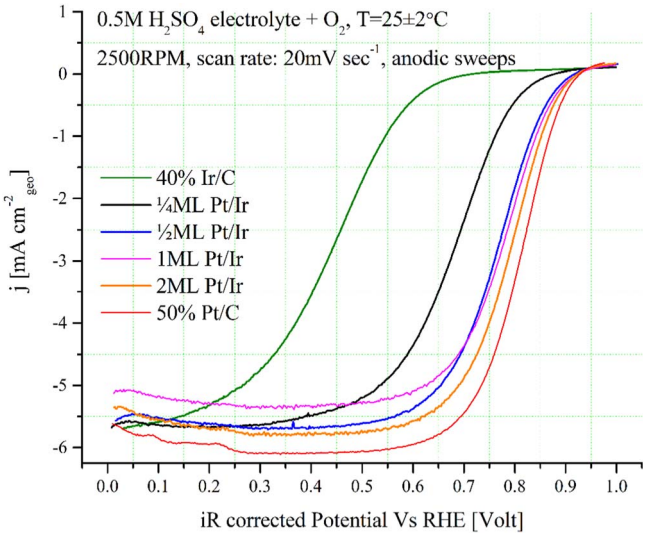

Figure 4. ORR polarization voltammograms of the studied catalysts.

Table II. ECSAs, ORR mass ($j_{MA}^{0.85V}$) and specific ($j_k^{0.85V}$) activities of the studied catalysts.

Catalyst	ECSA [$m^2\ g^{-1}_{PGM}$]	$j_{MA}^{0.85V}$ [$A\ g^{-1}_{Pt}$]	$j_k^{0.85V}$) [$A\ m^{-2}_{PGM}$]
50%Pt/C	49	124	2.53
40%Ir/XC72	34	0.9[a)]	0.026
¼ML Pt/Ir	35	132	0.36
½ML Pt/Ir	33	178	0.96
1 ML Pt/Ir[a)]	32	154	1.33
2 ML Pt/Ir	32	155	2.46

a) Expressed in $A\ g^{-1}_{Ir}$.

substantially lower, at only 0.9 $A\ g^{-1}_{Ir}$, when compared to Pt-containing catalysts.

The specific activities of the catalysts were determined to be 0.36 $A\ m^{-2}_{PtIr}$ for ¼ML Pt/Ir, 0.96 $A\ m^{-2}_{PtIr}$ for ½ML Pt/Ir, 1.33 $A\ m^{-2}_{PtIr}$ for 1 ML Pt/Ir, 2.46 $A\ m^{-2}_{PtIr}$ for 2 ML Pt/Ir, 2.53 $A\ m^{-2}_{Pt}$ for 50%Pt/C. Similarly to the mass activity results, the specific activity of 40%Ir/XC72 was notably lower than that of Pt-containing catalysts, measuring only 0.026 $A\ m^{-2}_{Ir}$.

Theoretical ORR activity estimation.—In this section we present the theoretical estimation of the ORR activity at nML Pt/Ir(111) (n = 0, 1, 2). We first calculate the binding energies of O and OH at those surfaces. We then perform CI-NEB calculations to estimate the transition state barriers for O_2 dissociation and OH formation at the surfaces. Finally, we use the resulting free energy changes and the energy barriers to estimate the ORR activity.

Binding energies.—We present the lowest energy structures for O and OH bound on nML Pt/Ir(111) (n = 0, 1, 2) and Pt(111) surfaces in Fig. 5. We found that O binds on hollow sites on nML Pt/Ir(111) (n = 0, 1, 2) and Pt(111), while OH binds on bridge site when it binds on Ir(111) and Pt(111) and on top-site when it binds on 1 ML and 2 ML of Pt/Ir(111). We did not perform simulations of partial monolayers since they have heterogeneous surface sites and a simple analysis of adsorption energies will not be representative of a real-world situation.

The results for the binding energies are presented in Fig. S4 and Table S1 in the SM. We found that our results for the binding energy, E_b, are in a good agreement with the results of Yang et al.[20] and Lu et al.[83] For example, Yang et al. reported binding energies of −4.37 eV for O binding and −2.52 eV for OH binding on Pt(111). Compared to our findings these values are slightly higher, by 0.09 eV, for O binding and slightly lower, by 0.03 eV, for OH binding. Interestingly, Yang et al. reported binding energies for O and OH binding on 1 ML and 2 ML of Pt/Ir(111) that are slightly lower than our results for 1 ML and 2 ML of Pt/Ir(111), exhibiting similar binding trends, i.e. the results reported by Yang et al. are −3.57 eV and −3.86 eV for O binding on 1 ML and 2 ML of Pt/Ir (111), respectively, while our results are −3.71 eV and −3.99 eV, respectively.

The binding energies of O and OH on Ir(111) surface are significantly higher than the ones for Pt(111) surface. These results are in an agreement with the experimentally known more oxophilic nature of iridium compared to platinum, that manifests itself in the lower potentials (∼350 mV) of iridium oxidation compared to oxidation of platinum (∼700 mV), as can be seen in Figs. 3b and 3a respectively.

Transition state barriers.—The results for the calculated ΔG s, the transition states barriers, $E_A^{O_2 diss.}$ and $E_A^{\ OHdiss.}$, and the resulting estimated activity, calculated using Eq. 8, are shown in Table III. The geometry of the initial and final states, for the various configurations, is shown in Figs. S5 and S6 in the SM. Our result for O_2 dissociation barrier on Pt(111), 0.55 eV, is in close agreement with the result of 0.54 eV of McEwen et al.[84] Our results for the transition state barrier for O_2 dissociation on Pt(111) and 1 ML Pt/Ir (111) surfaces (0.55 eV and 0.94 eV, respectively) show the same trend as shown by Nilekar et al.[26] (0.77 eV and 1.08 eV, respectively), i.e. this transition state barrier on 1 ML Pt/Ir(111) surface is higher than on Pt(111). Our results for the transition state barrier for OH formation on Pt(111) and 1 ML Pt/Ir(111) surfaces (0.64 eV and 0.60 eV, respectively) also show the same trend as Nilekar et al.[26] (0.86 eV and 0.67 eV, respectively). However, our results show a smaller difference between the transition state barriers of the two surfaces. Our result for the transition state barrier for O_2 dissociation on Ir(111), 0.1 eV, is in close agreement to the result of 0.06 eV of Yu and Mavrikakis.[85]

ORR activity.—The data presented in Table III makes it evident that the activity is governed by the transition states barriers. On the Ir (111) surface the limiting process, the one with the higher transition states barrier, is the OH formation. On the 1 ML Pt/Ir(111) and 2 ML Pt/Ir(111) surfaces the limiting process is the O_2 dissociation. We found the OH formation to be the limiting process on the Pt(111) surface. However, it's energy barrier is very close to the energy barrier of O_2 dissociation.

Figure 6 shows the estimated activity and the transition state barriers for O_2 dissociation and OH formation as a function of the calculated oxygen binding energy. It is clear from the figure that the O_2 dissociation energy exhibits a perfect linear relation to the binding energy, while the OH formation deviates a bit from a linear relation. This deviation from the linear scaling relationship can perhaps be explained by the fact the O binding site is the same on all surfaces, while the OH binding site changes from hollow on the clean surfaces to on top in the 1 ML and 2 ML surfaces. Figure 7 shows the estimated activity as a function of the transition state barriers for O_2 dissociation and OH formation.

Analysis of the experimentally measured and theoretically estimated catalytic activities.—We shall commence the analysis by examining the ORR specific activities. The specific activity of 40%Ir/XC72 stands out as notably lower, ranging from one to two orders of magnitude, compared to any other catalyst in this study (Table II). A similar two-order magnitude difference between the specific activities of Ir/C and Pt/C was reported by Yang et al.[86] As can be seen in Fig. 3b, due to its oxophilic nature, iridium begins to undergo oxidation at potentials as low as ∼350 mV. Consequently,

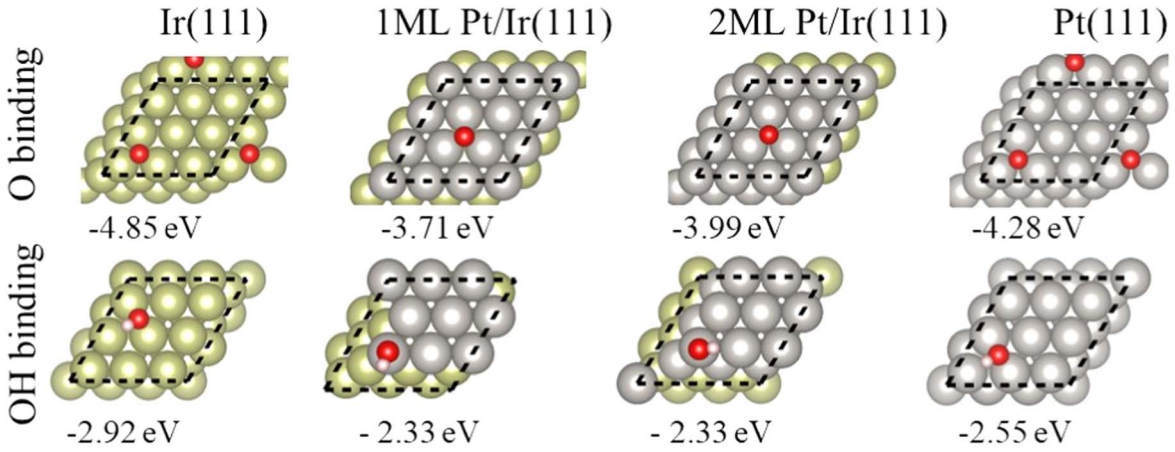

Figure 5. O and OH binding on nML Pt/Ir(111) (n = 0, 1, 2) and Pt(111) surfaces. The binding energies of O and OH on the surfaces are given below the figures.

Table III. Calculated ΔGs, transition state barriers and activities for the studied surfaces.

Surface	$\Delta G_0(U_0)$ [eV]	$\Delta G_1(U_0)$ [eV]	$\Delta G_2(U_0)$ [eV]	$E_A^{O_2diss.}$[eV]	$E_A^{OH\,form.}$[eV]	Activity [eV]
Ir(111)	−0.71	0.75	−0.04	0.10	1.07	−1.07
1 ML Pt/Ir(111)	0.41	0.20	−0.61	0.94	0.60	−0.94
2 ML Pt/Ir(111)	0.16	0.46	−0.62	0.76	0.65	−0.76
Pt(111)	−0.15	0.55	−0.40	0.55	0.64	−0.64

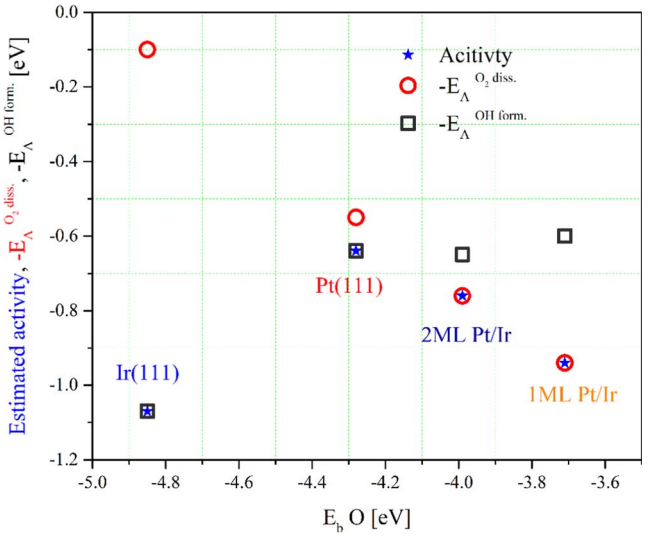

Figure 6. The estimated activity and the transition state barriers for O_2 dissociation ($E_A^{O_2diss.}$) and OH formation ($E_A^{OH\,form.}$) as a function of the calculated oxygen binding energy (E_b O).

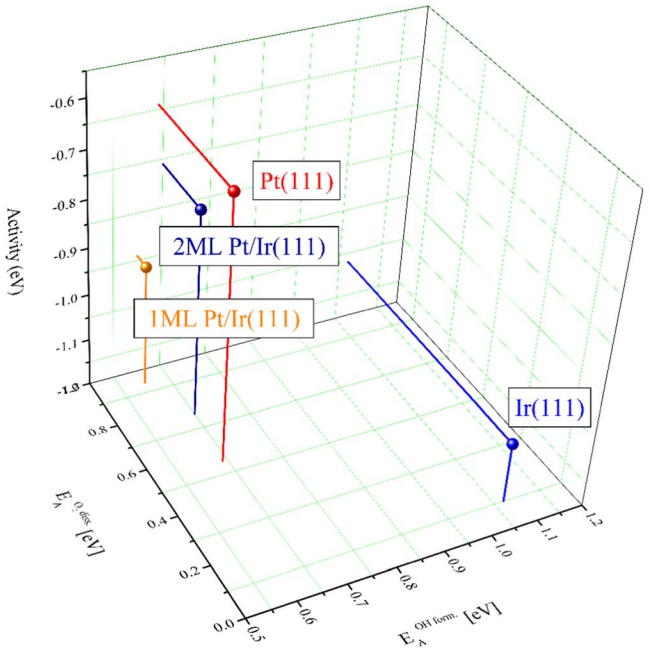

Figure 7. The estimated activity as a function of the transition state barriers for O_2 dissociation ($E_A^{O_2diss.}$) and OH formation ($E_A^{OH\,form.}$).

at a potential of 0.85 V, the surface of iridium is extensively oxidized, resulting in limited available surface area for the adsorption of O_2 molecules and their subsequent reduction. Furthermore, even at potentials typical for PEM-cathode operation during high current density, i.e., 0.6−0.7 V, considerably lower than 0.85 V, substantial oxidation of the iridium surface persists, impeding the adsorption of O_2 molecules. Below the potential of 0.6 V, the Ir-oxide coverage is sufficiently low, allowing for notable ORR currents to be obtained.

Our theoretical calculations also reflect the oxophilic characteristic of iridium, revealing a notably higher binding energy of O on the Ir(111) surface compared to other surfaces examined. It has been demonstrated that a high binding energy of an adsorbate facilitates bond-breaking steps when the adsorbate acts as a product but hampers bond-making steps when the adsorbate serves as a reactant.[26] Following the Sabatier principle, an optimal catalyst should exhibit a balanced adsorbate binding—neither excessively strong nor weak—to enable both bond-breaking and bond-making steps. In the context of iridium, this suggests that while O_2 molecules may readily dissociate if adsorbed on the surface, the formation of OH, which necessitates a bond-making step, will be notably impeded, posing a bottleneck in the ORR process. Transition state

barriers for O_2 dissociation and OH formation on Ir(111) illustrate this phenomenon; while the barrier for O_2 dissociation is comparatively lower for Ir(111) than the other surfaces, the barrier for OH formation is substantially higher, ultimately dictating the estimated ORR activity (Table III). Consequently, Ir(111) exhibits the lowest estimated activity among the surfaces examined, which aligns well with the observed low ORR specific activity of 40%Ir/XC72.

The specific activity of 50%Pt/C stands out as the highest among the catalysts studied, albeit slightly higher than that of 2 ML Pt/Ir. Regarding the availability of the surface for O_2 molecule adsorption and dissociation, Fig. 3a illustrates that the platinum surface at 0.85 V is partially oxidized, thus relatively accessible. The theoretical calculations for Pt(111) closely align with the experimental findings for 50%Pt/C. Notably, the binding energy of O on the Pt (111) surface is considerably lower than that on Ir(111), resulting in a slower O_2 dissociation process on Pt(111). However, OH formation on Pt(111) occurs significantly faster. This balance between O_2 dissociation and OH formation processes on Pt(111), compared to Ir (111), is evident in the transition state barriers, ultimately leading to a higher estimated activity for Pt(111).

One might anticipate that the specific activity of 1 ML Pt/Ir would resemble that of 50%Pt/C. However, this is not the case; the specific activity for 1 ML Pt/Ir falls approximately midway between those of 40%Ir/XC72 and 50%Pt/C. Firstly, the voltammogram of 1 ML Pt/Ir (Fig. 3c) suggests the presence of iridium on its surface, a conclusion supported by the STEM-EDS mapping of this catalyst (Fig. 2c). Consequently, the specific activity of 1 ML Pt/Ir includes a contribution not only from the platinum layer but also from the iridium core as well, which exhibits very low activity. Secondly, the theoretical calculations imply that the specific activity of platinum is negatively affected by the iridium core. The binding energy of O on 1 ML Pt/Ir(111) is significantly lower than on Pt(111), resulting in slower O_2 dissociation on 1 ML Pt/Ir(111) compared to Pt(111). Indeed, the transition state barrier for O_2 dissociation on 1 ML Pt/Ir (111) is the highest among all the studied surfaces and governs its estimated activity. Nilekar et al.[26] attributed the lower binding energy of O on 1 ML Pt/Ir(111) compared to Pt(111) to the compressive strain induced on the platinum layer by the iridium substrate. This strain results in a lower d-band center, thereby weakening the binding of O.

The specific activity of 2 ML Pt/Ir falls within the margin of error of 50%Pt/C and is significantly higher than that of 1 ML Pt/Ir. The high specific activity of 2 ML Pt/Ir, compared to 1 ML Pt/Ir, can be attributed to the absence of negative contributions from exposed iridium surfaces, unlike in the case of 1 ML Pt/Ir, and the reduced adverse effect of the iridium core on the topmost platinum layer. Theoretical calculations align well with experimental findings when comparing 1 ML and 2 ML Pt/Ir(111) surfaces to 1 ML and 2 ML Pt/Ir catalysts. The binding energy of O on 2 ML Pt/Ir(111) exceeds that of 1 ML Pt/Ir(111), resulting in a lower transition state barrier for O_2 dissociation on 2 ML Pt/Ir(111) compared to 1 ML Pt/Ir(111). This difference governs the estimated activity for both surfaces, leading to a significantly higher estimated activity on 2 ML Pt/Ir (111) than on 1 ML Pt/Ir(111), mirroring the higher specific activity of 2 ML Pt/Ir compared to 1 ML Pt/Ir.

In comparison to Pt(111), the binding energy of O on 2 ML Pt/Ir (111) is lower and the transition state barrier for O_2 dissociation is higher. A probable explanation for the lower binding energy of O on 2 ML Pt/Ir(111) compared to Pt(111) is the compressive strain induced by the iridium substrate, similar to what occurs with 1 ML Pt/Ir(111). However, this compressive strain is likely to be less pronounced for 2 ML Pt/Ir(111) than for 1 ML Pt/Ir(111), resulting in the lower binding energy of O on 2 ML Pt/Ir(111).

The transition state barrier for O_2 dissociation on 2 ML Pt/Ir(111) is higher than that for OH formation on Pt(111), which according to the calculations governs the estimated activity on the latter surface. Consequently, the estimated activity on 2 ML Pt/Ir(111) is lower compared to Pt(111). While the specific activities of 2 ML Pt/Ir and 50%Pt/C are similar, there exists a notable variance between the theoretically estimated activities of 2 ML Pt/Ir(111) and Pt(111) surfaces. This can be attributed to the limitations of the modeled surfaces in accurately representing actual nanoparticles. Figure 4 and the data in Table II illustrate that even a small addition of platinum to iridium, equivalent to ¼ monolayer, leads to a significant increase in specific activity; the specific activity of ¼ML Pt/Ir surpasses that of 40%Ir/XC72 by an order of magnitude, reaching 0.36 A m^{-2}_{PGM}

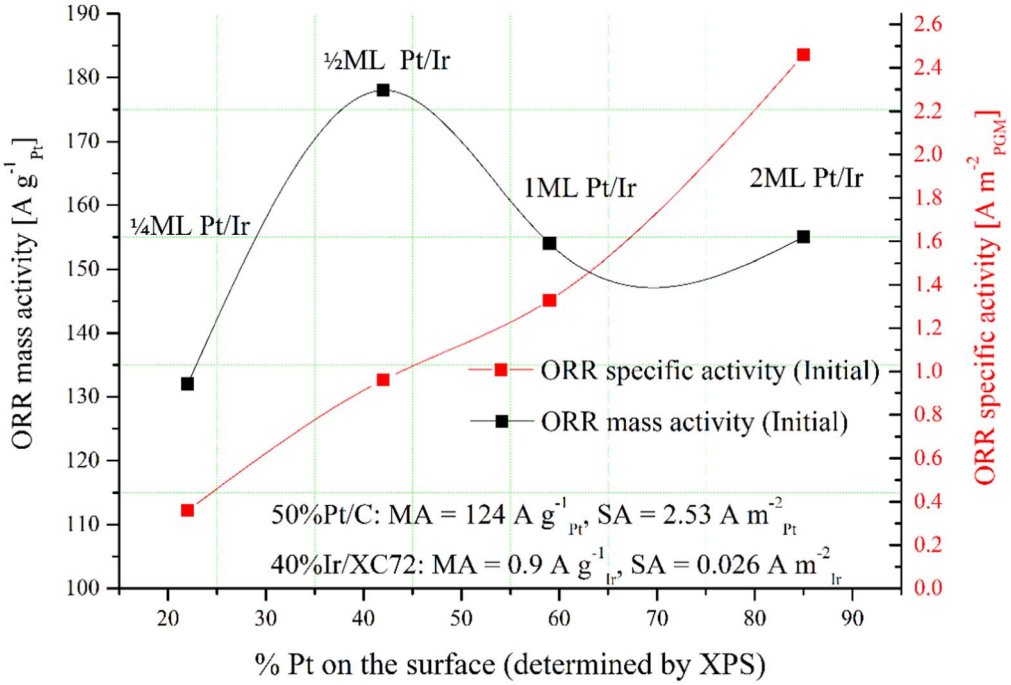

Figure 8. The catalytic activity of Pt/Ir catalysts plotted against the %Pt on the surface, derived from XPS analysis. Mass activities are depicted by the black curve, while specific activities are shown by the red curve. Data for 50%Pt/C and 40%Ir/XC72 are included for comparative purposes. Abbreviations: MA = mass activity, SA = surface activity.

Table IV. ORR mass activities ($j_{MA}^{0.85V}$) before and after AST.

Catalyst	$j_{MA}^{0.85V}$ before AST [A g^{-1}_{Pt}]	$j_{MA}^{0.85V}$ after AST [A g^{-1}_{Pt}]	Decrease in $j_{MA}^{0.85V}$ after AST
50%Pt/C	124	99	20%
40%Ir/XC72	0.9[a)]	0.4[a)]	55%
¼ML Pt/Ir	132	81	39%
½ML Pt/Ir	178	137	23%
1 ML Pt/Ir	154	140	9%
2 ML Pt/Ir	155	124	20%

a) Expressed in A g^{-1}_{Ir}.

Table V. ORR specific activities ($j_k^{0.85V}$) before and after AST.

Catalyst	$j_k^{0.85V}$ before AST [A m^{-2}_{PGM}]	$j_k^{0.85V}$ after AST [A m^{-2}_{PGM}]	Decrease in $j_k^{0.85V}$ after AST
50%Pt/C	2.53	2.42	4%
40%Ir/XC72	0.026	0.015	42%
¼ML Pt/Ir	0.36	0.27	25%
½ML Pt/Ir	0.96	0.86	10%
1 ML Pt/Ir	1.33	1.33	0%
2 ML Pt/Ir	2.46	2.34	5%

compared to 0.028 A m^{-2}_{Ir}, indicating that more than 90% of the ORR occurs on the platinum surface. Further, for ½ML Pt/Ir, the specific activity increases by approximately 2.5 times to 0.96 A m^{-2}_{PGM}. These specific activities are notably lower than that of 50%Pt/C, as expected, given that a significant portion of the surface of ¼ML Pt/Ir and ½ML Pt/Ir consists of iridium, which exhibits a very low specific activity.

In summarizing the specific activity analysis, it becomes evident that the specific activity rises with a higher platinum content on the surface (depicted by the red curve in Fig. 8). This increase is attributed to the transition in surface composition from predominantly iridium to platinum, which is significantly more catalytically active. Initially, the catalytic activity of the first layer of platinum atoms atop iridium is hindered by the presence of the iridium core. However, this negative effect diminishes with additional layers of platinum, resulting in a subsequent increase in specific activity.

In contrast to the trend observed in specific activity with increasing platinum content on the surface, the mass activity (depicted by the black curve in Fig. 8) shows an increase for ½ML Pt/Ir, followed by a decline for 1 ML Pt/Ir, and a slight increase for 2 ML Pt/Ir. This pattern arises from the intricate interplay between specific activity and platinum utilization. While the specific activity increases with more platinum on the surface, the formation of platinum bi-layers reduces platinum utilization. Notably, ½ML Pt/Ir, exhibiting the highest mass activity (178 A g^{-1}_{Pt}), represents the optimal balance between specific activity and platinum utilization.

Despite exhibiting lower specific activities, the ½ML Pt/Ir and 1 ML Pt/Ir catalysts showcased higher mass activities than that of 50%Pt/C by 43% and 24%, respectively. Similarly, the mass activity of 2 ML Pt/Ir catalysts exceeded that of 50%Pt/C by 25%, despite their similar specific activities. These findings underscore the significant potential of core–shell structures in enhancing the platinum utilization of ORR catalysts, even in scenarios where platinum is influenced negatively by the core metal.

Table VI. ECSA before and after AST.

Catalyst	ECSA before AST [m^2 g^{-1}_{PGM}]	ECSA after AST [m^2 g^{-1}_{PGM}]	Decrease in ECSA after AST
50%Pt/C	49	41	16%
40%Ir/XC72	34	27	21%
¼ML Pt/Ir	35	28	20%
½ML Pt/Ir	33	28	15%
1 ML Pt/Ir	32	29	10%
2 ML Pt/Ir	32	27	15%

Analysis of the catalyst durability.—Table IV presents a comparison of the ORR mass activities normalized for platinum weight, both before and after AST. Tables V and VI provide a comparison of the specific activities and ECSA values of the studied catalysts before and after AST.

The highest decrease in mass activity was observed in 40%Ir/XC72 (55%), followed by ¼ML Pt/Ir (39%). Conversely, 1 ML Pt/Ir exhibited the lowest decrease at only 9%. The decrease in mass activity for ½ML Pt/Ir, 2 ML Pt/Ir, and 50%Pt/C was comparable, ranging from 23% to 20%. A similar pattern emerges when examining the decrease in ECSA values: 40%Ir/XC72 and ¼ML Pt/Ir experienced the most significant decreases, followed by ½ML Pt/Ir, 2 ML Pt/Ir, and 50%Pt/C, which exhibited similar decreases, while 1 ML Pt/Ir demonstrated the smallest decrease.

Given the superior durability demonstrated by 1 ML Pt/Ir, which resulted in its highest mass activity post-AST, and taking into account the imperative for long term operation of PEMFCs, it becomes apparent that among the studied Pt/Ir catalysts, 1 ML Pt/Ir stands out as the most feasible choice for practical use in PEMFCs.

Through years of studying the durability of PGM-based carbon-supported ORR catalysts, carbon corrosion, PGM dissolution and redeposition (the so-called Ostwald ripening), and coalescence caused by particle migration were identified as the primary degradation mechanisms. A study by Urchaga et al. indicated that carbon corrosion is negligible during AST with a UPL of 0.9 V.[87] Therefore, given the same UPL used in this study, it can be inferred that the degradation observed in the studied catalysts due to carbon corrosion in minimal. Furthermore, since all the studied catalysts share a similar type of carbon support, it can be inferred that the level of coalescence via particle migration during AST is also similar. Consequently, it is reasonable to assume that among the three degradation mechanisms mentioned above, the one responsible for the decrease in the mass activities and ECSAs of the catalysts is the dissolution and redeposition of platinum and iridium. This process typically results in the loss of the metals into the electrolyte and the growth of catalyst particles.

DFT studies have demonstrated that the Pt-Ir bond exhibits greater strength than both Pt-Pt and Ir-Ir bonds.[36] Furthermore, these studies have predicted the stabilization of platinum when deposited on an iridium substrate.[37,38] These findings suggest that the dissolution rate of platinum atoms directly in contact with the iridium core will be slower than those not in direct contact. As can be concluded from the STEM-EDS mappings, the platinum on the surface of 1 ML Pt/Ir is primarily deposited directly onto iridium, while the platinum on the surface of 2 ML Pt/Ir forms platinum multilayers, with the topmost platinum layer not in direct contact with iridium. Naturally, in 50%Pt/C platinum is the only metal, precluding any possibility of platinum-iridium contact. Consequently, a slower platinum dissolution in 1 ML Pt/Ir may account for its lower decrease in mass activity and ECSA compared to 50%Pt/C and 2 ML Pt/Ir.

However, the slower platinum dissolution cannot explain the lower mass activity decrease of 1 ML Pt/Ir compared to ¼ML Pt/Ir and ½ML Pt/Ir, given that all three catalysts feature platinum atoms that are primarily in contact with the iridium core. One possible explanation could be attributed to the high amount of iridium exposed on the surfaces of ¼ML Pt/Ir and ½ML Pt/Ir. This exposure may lead to considerable iridium dissolution, potentially leading to the detachment of platinum atoms from the iridium core.

An examination of the specific activities before and after AST (Table V) reveals an interesting picture, suggesting an additional factor contributing to the greater mass activity decrease of ¼ML Pt/Ir and ½ML Pt/Ir. It can be said that, within a margin of error, the specific activities of 1 ML Pt/Ir, 2 ML Pt/Ir and 50%Pt/C remained constant following AST. However, the specific activities of ½ML Pt/Ir, ¼ML Pt/Ir and 40%Ir/XC72 decreased by 10%, 25% and 42%, respectively.

The decrease in the specific activity exhibited by ½ML Pt/Ir and ¼ML Pt/Ir may be attributed to a change in their surface composition. While the exposed iridium on their surface is expected to lead to a significant iridium dissolution, the dissolution of platinum is expected to be lower due to its stabilization by the iridium core. This would lead to high concentration of iridium ions in the electrolyte in the vicinity of the nanoparticles. It is likely that during the redeposition stage of the Ostwald ripening, some iridium ions will redeposit onto the surface of the topmost platinum atoms of the nanoparticles, thereby increasing the iridium content on the surface and modifying its surface composition. Thus, we speculate that in the case of these two catalysts, platinum and iridium dissolution has not only led to their loss into the electrolyte and particle growth via Ostwald ripening but also to an increased iridium content on the surface of the catalysts. Such a change of the surface composition would decrease the number of active platinum sites on the surface, consequently reducing the specific activity of the catalysts. Given the relationship between mass activity and specific activity, the mass activity is also expected to be negatively affected. Generally, this change in the surface composition can be relevant also for 2 ML Pt/Ir and 1 ML Pt/Ir catalysts during longer AST protocols.

One would expect to see evidence of increased iridium content on the surface of ½ML Pt/Ir and ¼ML Pt/Ir in their voltammograms after AST (Fig. S3). However, examination of these voltammograms do not indicate any perceptible changes in the surface composition of these catalysts. This lack of evidence could be attributed to the subtle nature of these changes, which might not be significant enough to manifest visibly on the voltammograms, especially considering that their overall shape is already predominantly influenced by a high iridium content on the catalyst surface.

Obviously, increase in the iridium content on the surface cannot explain the decrease in the specific activity of 40%Ir/XC72. This decrease can be attributed to the irreversible oxidation of iridium, as demonstrated in the experimental section, which occurs during potential cycling to sufficiently high UPLs. This oxidation of the iridium surface hinders the adsorption of O_2 molecules, thereby diminishing its specific activity. The irreversible oxidation of iridium would also contribute to the decrease in the ECSA of 40% Ir/XC72, as oxidized iridium cannot adsorb hydrogen through underpotential deposition. Looking back at ½ML Pt/Ir and ¼ML Pt/Ir, given the high iridium content on their surface, iridium oxidation can be an additional mechanism, besides PGM dissolution, causing the decrease of their ECSAs.

To summarize the analysis of the durability of the catalysts, we propose that the decrease in the mass activity of the catalysts can be attributed to the following mechanisms:

a. For 40%Ir/XC72: iridium dissolution and surface oxidation.
b. For ¼ML Pt/Ir and ½ML Pt/Ir: dissolution of platinum and iridium, with subsequent redeposition of iridium on platinum.
c. For 1 ML Pt/Ir, 2 ML Pt/Ir, and 50%Pt/C: primarily platinum dissolution, with a possibility of some iridium dissolution in the case of 1 ML Pt/Ir. The enhanced durability of 1 ML Pt/Ir is attributed to the stabilization of the platinum shell by the iridium core.

It must be noted that since we were unable to examine the catalysts by TEM, STEM-EDS mapping and XPS following AST procedures, we weren't able to verify changes in their particle sizes and surface compositions.

As outlined in the introduction, addressing cost and durability represents two pivotal challenges in advancing the commercialization of PEMFC technology. The findings presented in this study offer a potential solution to the durability challenge, particularly in reducing platinum dissolution. However, it is crucial to consider the implications for catalyst cost when using a Pt/Ir system. Currently, the cost of iridium surpasses that of platinum. Iridium is heavily used in PEM electrolyzers as a catalyst in the oxygen evolution reaction. Moreover, iridium is less abundant than platinum. Consequently, cost wise, the Pt/Ir system, with iridium as a core material, is challenging for practical fuel cell applications. A more viable approach would involve using iridium as an interlayer between a core comprised of a substantially more cost-effective material and an outer shell composed of platinum.

Conclusions

In this work we systematically studied the ORR activity and durability of Pt/Ir catalysts as a function of platinum content. Four catalysts were synthesized, featuring platinum shell equivalent to ¼ML, ½ML, 1 ML, and 2 ML on iridium nanoparticles.

Examination of the nanostructure of the synthesized catalysts, by STEM-EDS mapping and CV, verified the formation of partial to complete platinum shells on the iridium cores.

The specific activity of the synthesized catalysts showed an increase with the incremental addition of platinum to the nanoparticle shell. The factors influencing the ORR activities of both the synthesized catalysts and the commercial 50%Pt/C and 40%Ir/XC72 catalysts were clarified by examining the ORR activity on nML Pt/Ir (111), Pt(111), and Ir(111) surfaces through DFT simulations. Both experimental and theoretical results showed that the specific activity of the initial layer of platinum atoms on the iridium surface is impeded by the presence of iridium. However, this negative effect diminished with the addition of more platinum layers, leading to a subsequent enhancement in specific activity, approaching that of 50%Pt/C. Despite their specific activities being lower or similar compared to 50%Pt/C, the ½ML Pt/Ir, 1 ML Pt/Ir, and 2 ML Pt/Ir catalysts displayed higher mass activities than 50%Pt/C. These results demonstrate the superior platinum utilization of core–shell structures.

Durability study showed that the 1 ML Pt/Ir catalyst exhibited the lowest decrease in ORR mass activity, approximately two times lower compared to 50%Pt/C, 2 ML Pt/Ir and, ½ML Pt/Ir catalysts. At the same time, ¼ML Pt/Ir and 40%Ir/XC72 catalysts exhibited significantly higher decrease in mass activity, more than four and five times higher (respectively) compared to 1 ML Pt/Ir. The decrease in the ECSAs of the catalysts followed a generally similar trend. The decrease in mass activity of ½ML Pt/Ir, ¼ML Pt/Ir and 40%Ir/XC72 was accompanied by a decrease in their specific activity.

The decrease observed in the mass and specific activities, as well as the ECSAs of the studied catalysts, was attributed to platinum and iridium dissolution, iridium redeposition on platinum, and irreversible oxidation of iridium. The high durability of 1 ML Pt/Ir was explained by the slower dissolution of platinum, facilitated by its stabilization by iridium. The highest mass activity of 1 ML Ir/Pr post-AST makes it the most suitable choice for application in PEMFCs among the four synthesized catalysts.

However, considering the high cost and low abundance of iridium, as well as its usage in PEM-electrolyzers, implementing it as a core material poses practical challenges. Therefore, to practically implement the promising findings demonstrated by 1 ML Pt/Ir,

it would involve reducing the quantity of iridium by employing it as an interlayer between a platinum shell and a core composed of a more cost-effective and widely available material.

Acknowledgments

The authors wish to thank the Directorate of Defense Research & Development of the Israel Ministry of Defense, the Israel Ministry of Energy, the Planning & Budgeting Committee of the Council of High Education, and the Prime Minister Office of Israel (in the framework of the INREP project) for financial support provided for this research.

ORCID

D. Kaplan https://orcid.org/0000-0001-8179-2238
M. Shviro https://orcid.org/0000-0002-9494-0233
E. Peled https://orcid.org/0000-0001-6949-553X

References

1. V. S. Bagotsky (ed.), *Fuel Cells: Problems and Solutions* 2nd ed. (Wiley Ltd.) (2012).
2. M. Z. Jacobson, W. G. Colella, and D. M. Golden, "Cleaning the air and improving health with hydrogen fuel-cell vehicles." *Science*, **308**, 1901 (2005).
3. M. K. Debe, *Nature*, **486**, 43 (2012).
4. R. Borup and A. Weber, "FC-PAD: fuel cell performance and durability consortium." *DOE Fuel Cell Technologies Office Annual Merit Review*, **2020** (2020), Accessed at 16/11/2023.
5. A. Weber, "M2FCT: million mile fuel cell truck consortium." *DOE Hydrogen Fuel Cell Technologies Office 2023 Annual Merit Review, June 2020, Accessed at 16/11/2023*.
6. J. Marcinkoski, R. Vijayagopal, J. Adams, B. James, J. Kopasz, and R. Ahluwalia, "DOE Advanced Truck Technologies, Subsection of the Electrified Powertrain Roadmap." *Technical Targets for Hydrogen-Fueled Long-Haul Tractor-Trailer Trucks* (2019), Accessed at 16/11/2023.
7. O. Gröger, H. A. Gasteiger, and J. P. Suchsland, *J. Electrochem. Soc.*, **162**, A2605 (2015).
8. D. Banham, Y. Peng, J. Bai, J. Choi, W. Huancheng, and M. E. A. Cost, "Reduction through manufacturing approaches and materials level innovation." *Proceedings of EFCF 2023 low-Temperature Electrolysers, Fuel Cells & H2 Processing*.
9. M. K. Debe, "Electrocatalyst approaches and challenges for automotive fuel cells." *Nature*, **486**, 43 (2012).
10. O. Gröger, H. A. Gasteiger, and J.-P. Suchsland, "Electromobility: batteries or fuel cells?" *J. Electrochem. Soc.*, **162**, A2605 (2015).
11. H. A. Gasteiger, S. Kocha, B. Sompalli, and F. Wagner, "Activity benchmarks and requirements for Pt, Pt-Alloy, and Non-Pt oxygen reduction catalysts for PEMFCs." *Appl. Catalysis B*, **56**, 9 (2005).
12. J. Zhang, *PEM Fuel Cells and Platinum-Based Electrocatalysts in Fuel Cells - Selected Entries from the Encyclopedia of Sustainability Science and Technology*, ed. K. D. Kreuer (Springer Science + Business Media, New York) p. 305 (2013).
13. A. Rabis, P. Rodriguez, and T. J. Schmidt, "Electrocatalysis for polymer electrolyte fuel cells: recent achievements and future challenges." *ACS Catal.*, **2**, 864 (2012).
14. D. Li, H. Lv, Y. Kang, N. M. Markovic, and V. R. Stamenkovic, "Progress in the development of oxygen reduction reaction catalysts for low-temperature fuel cells." *Annual Review of Chemical and Biomolecular Engineering*, **7**, 509 (2016).
15. M. Shao, Q. Chang, J.-P. Dodelet, and R. Chenitz, "Recent advances in electrocatalysts for oxygen reduction reaction." *Chem. Rev.*, **116**, 3594 (2016).
16. D. Banham and S. Ye, "Current status and future development of catalyst materials and catalyst layers for proton exchange membrane fuel cells: an industrial perspective." *ACS Energy Lett.*, **2**, 629 (2017).
17. H. Li, H. Zhao, B. Tao, G. Xu, S. Gu, G. Wang, and H. Chang, "Pt-Based oxygen reduction reaction catalysts in proton exchange membrane fuel cells: controllable preparation and structural design of catalytic layer." *Nanomaterials*, **12**, 4173 (2022).
18. J. X. Wang, H. Inada, L. Wu, Y. Zhu, Y. M. Choi, P. Liu, W. P. Zhou, and R. R. Adzic, "Oxygen reduction on well-defined core–shell nanocatalysts: particle size, facet, and Pt Shell thickness effects." *J. American Chemical Soc.*, **131**, 17298 (2009).
19. S. L. Knupp, M. B. Vukmirovic, P. Haldar, J. A. Herron, M. Mavrikakis, and R. R. Adzic, "Design and development of highly active, nanoengineered, platinum-based core–shell electrodes for proton exchange membrane fuel cells." *Electrocatalysis*, **1**, 213 (2010).
20. L. Yang, M. B. Vukmirovic, D. Su, K. Sasaki, J. A. Herron, M. Mavrikakis, S. Liao, and R. R. Adzic, "Tuning the catalytic activity of Ru@Pt core–shell nanoparticles for the oxygen reduction reaction by varying the shell thickness." *J. Phys. Chem. C*, **117**, 1748 (2013).
21. Y. Kang, J. Snyder, M. Chi, D. Li, K. L. More, N. M. Markovic, and V. R. Stamenkovic, "Multimetallic core/interlayer/shell nanostructures as advanced electrocatalysts." *Nano Lett.*, **14**, 6361 (2014).
22. A. Kongkanand, N. P. Subramanian, Y. Yu, Z. Liu, H. Igarashi, and D. A. Muller, "Achieving high-power PEM fuel cell performance with an Ultralow-Pt-Content Core–shell catalyst." *ACS Catal.*, **6**, 1578 (2016).
23. S. Mukerjee, S. Srinivasan, M. P. Soriaga, and J. McBreen, *J. Electrochem. Soc.*, **142**, 1409 (1995).
24. S. Ball, "Core–shell catalysts in PEMFC cathode environments." *Electrocatalysis in Fuel Cells: A Non- and Low- Platinum Approach*, ed. M. Shao (Springer, London) p. 561 (2013).
25. K. Sasaki, J. X. Wang, H. Naohara, N. Marinkovic, K. L. More, H. Inada, and R. R. Adzic, "Recent advances in platinum monolayer electrocatalysts for oxygen reduction reaction: scale-up synthesis, structure and activity of Pt shells on Pd cores." *Electrochim. Acta*, **55**, 2645 (2010).
26. A. U. Nilekar, Y. Xu, J. Zhang, M. B. Vukmirovic, K. Sasaki, R. R. Adzic, and M. Mavrikakis, "Bimetallic and ternary alloys for improved oxygen reduction catalysis." *Top. Catal.*, **46**, 276 (2007).
27. Y. Zhang, Y. C. Hsieh, V. Volkov, D. Su, W. An, R. Si, Y. Zhu, Y. Liu, J. X. Wang, and R. R. Adzic, "High performance Pt monolayer catalysts produced via Core–catalyzed coating in ethanol." *ACS Catal.*, **4**, 738 (2014).
28. K. Sasaki, H. Naohara, Y. Cai, Y. M. Choi, P. Liu, M. B. Vukmirovic, J. X. Wang, and R. R. Adzic, "Core-protected platinum monolayer shell high stability electrocatalysts for fuel-cell cathodes." *Angew. Chem. Int. Ed.*, **49**, 8602 (2010).
29. Y. Dong, Z. Li, G. Zheng, J. Zhang, J. Zhou, Y. Orikasa, Y. Uchimoto, and X. Wang, "Observing the structural evolution of quasi-monolayer Pt shell on Pd core in the electrocatalytic oxygen-reduction reaction." *The Journal of Physical Chemistry Letters*, **14**, 7027 (2023).
30. M. Zeng, Wang, Z. H. Tan, X. X. Huang, and J. N. Wang, "Remarkable durability of Pt–Ir alloy catalysts supported on graphitic carbon nanocages." *J. Power Sources*, **264**, 272 (2014).
31. S. Lu, K. Eid, Y. Deng, J. Guo, L. Wang, H. Wang, and H. Gu, "One-pot synthesis of PtIr tripods with a dendritic surface as an efficient catalyst for the oxygen reduction reaction." *J. Mater. Chem. A*, **5**, 9107 (2017).
32. J. Hu, K. A. Kuttiyiel, K. Sasaki, D. Su, T.-H. Yang, G.-G. Park, C. Zhang, G. Chen, and R. R. Adzic, "Pt monolayer shell on nitrided alloy core—a path to highly stable oxygen reduction catalyst." *Catalysts*, **5**, 1321 (2015).
33. P. P. Lopes et al., "Eliminating dissolution of platinum-based electrocatalysts at the atomic scale." *Nat. Mater.*, **19**, 1207 (2020).
34. H. Nan, Y.-Q. Su, C. Tang, R. Cao, D. Li, J. Yu, Q. Liu, Y. Deng, and X. Tian, "Engineering the electronic and strained interface for high activity of $PdM_{core}@Pt_{monolayer}$ electrocatalysts for oxygen reduction reaction." *Sci. Bull.*, **65**, 1396 (2020).
35. H. Wu, F. Xiao, J. Wang, M. Gu, and M. Shao, "Highly active and durable core–shell electrocatalysts for proton exchange membrane fuel cells." *Nano Res.* (2023).
36. Y. Le Page, C. Bock, and J. R. Rodgers, "Small step graphs of cell data versus composition for ccp solid-solution binary alloys: application to the (Pt,Ir), (Pt,Re) and (Pt,Ru) systems." *J. Alloys Compd.*, **422**, 164 (2006).
37. J. Greeley and J. K. Norskov, "Electrochemical dissolution of surface alloys in acids: Thermodynamic trends from first-principles calculations." *Electrochim. Acta*, **52**, 5829 (2007).
38. G. E. Ramírez-Caballero, Y. Ma, R. Callejas-Tovar, and P. B. Balbuena, "Surface segregation and stability of core–shell alloy catalysts for oxygen reduction in acid medium." *Phys. Chem. Chem. Phys.*, **12**, 2209 (2010).
39. N. Todoroki, H. Watanabe, T. Kondo, S. Kaneko, and T. Wadayama, "Highly enhanced oxygen reduction reaction activity and electrochemical stability of Pt/Ir (111) bimetallic surfaces." *Electrochim. Acta*, **222**, 1616 (2016).
40. A. L. Strickler, A. Jackson, and T. F. Jaramillo, "Active and stable Ir@Pt core–shell catalysts for electrochemical oxygen reduction." *ACS Energy Lett.*, **2**, 244 (2017).
41. A. J. Steinbach, "Highly active, durable, and ultra-low PGM NSTF thin film ORR catalysts and supports, U.S. D.O.E. hydrogen and fuel cell program." *2019 Annual Merit Review and Peer Evaluation, Accessed at 12/01/2021*.
42. D. Fang, X. Tang, L. Yang, D. Xu, H. Zhang, S. Sun, Z. Shao, and B. Yi, "Facile synthesis of Pt-decorated Ir black as a bifunctional oxygen catalyst for oxygen reduction and evolution reactions." *Nanoscale*, **11**, 9091 (2019).
43. H. B. Zheng, L. An, Y. Zheng, C. Qu, Y. Fang, Q. Liu, and D. Dang, "Tuning the catalytic activity of Ir@Pt nanoparticles through controlling ir core size on cathode performance for PEM fuel cell application." *Front. Chem.*, **6**, 299 (2018).
44. D. Kaplan, M. Goor, M. Alon, S. Tsizin, L. Burstein, Y. Rosenberg, I. Popov, and E. Peled, "Comparison of iridium–and ruthenium–based, Pt–surface–enriched, nanosize catalysts for the oxygen–reduction reaction." *J. Power Sources*, **306**, 219 (2016).
45. D. Kaplan, M. Goor, L. Burstein, I. Popov, M. Shviro, and E. Peled, "Increasing durability of Pt-surface-enriched nanosize structure catalysts by multi-step platinum deposition." *J. Solid State Electrochem.*, **24**, 2385 (2020).
46. L. Yang, M. B. Vukmirovic, D. Su, K. Sasaki, J. A. Herron, M. Mavrikakis, S. Liao, and R. R. Adzic, *J. Phys. Chem. C*, **117**, 1748 (2013).
47. F. Fiévet, S. Ammar-Merah, R. Brayner, F. Chau, M. Giraud, F. Mammeri, J. Peron, J. Y. Piquemal, L. Sicard, and G. Viau, "The polyol process: a unique method for easy access to metal nanoparticles with tailored sizes, shapes and compositions." *Chem. Soc. Rev.*, **47**, 5187 (2018).
48. J. K. Nørskov, J. Rossmeisl, A. Logadottir, L. Lindqvist, J. R. Kitchin, T. Bligaard, and H. Jonsson, *J. Phys. Chem. B*, **108**, 17886 (2004).
49. D. Kaplan, P. Tereshchuk, C. Olewsky, L. Keinan, O. Ben-Yehuda, M. Shviro, A. Natan, and E. Peled, "Study of ruthenium-contamination effect on oxygen reduction activity of platinum-based PEMFC and DMFC cathode catalyst." *J. Electrochem. Soc.*, **169**, 014517 (2022).
50. I. Takahashi and S. S. Kocha, *J. Power Sources*, **195**, 6312 (2010).
51. Y. Garsany, O. A. Baturina, K. E. Swider-Lyons, and S. S. Kocha, *Anal. Chem.*, **82**, 6321 (2010).

52. Y. Garsany, I. L. Singer, and K. E. Swider-Lyons, *J. of Electroanalytical Chemistry*, **662**, 396 (2011).
53. K. Shinozaki, J. W. Zack, S. Pylypenko, B. S. Pivovar, and S. S. Kocha, *J. Electrochem. Soc.*, **162**, F1384 (2015).
54. K. Shinozaki, J. W. Zack, R. M. Richards, B. S. Pivovar, and S. S. Kocha, *J. Electrochem. Soc.*, **162**, F1144 (2015).
55. D. A. J. Rand and R. Woods, "Cyclic voltammetric studies on iridium electrodes in sulphuric acid solutions: nature of oxygen layer and metal dissolution." *J. Electroanal. Chem. Interfacial Electrochem.*, **55**, 375 (1974).
56. J. Mozota and B. E. Conway, "Surface and bulk processes at oxidized iridium electrodes—I. Monolayer stage and transition to reversible multilayer oxide film behavior." *Electrochim. Acta*, **28**, 1 (1983).
57. S. Cherevko, S. Geiger, O. Kasian, A. Mingers, and K. J. J. Mayrhofer, "Oxygen evolution activity and stability of iridium in acidic media. Part 1.—Metallic iridium." *J. Electroanal. Chem.*, **773**, 69 (2016).
58. F. Nart and W. Vielstich, "Normalization of porous active surfaces in handbook of fuel cells - fundamentals." *Technology and Applications* Ch. 21 Vol. 2, ed. W. Vielstich et al. (Wiley, Ltd.) (2003).
59. R. Woods, "Hydrogen adsorption on platinum, iridium and rhodium electrodes at reduced temperatures and the determination of real surface area." *J. Electroanal. Chem. Interfacial Electrochem.*, **49**, 217 (1974).
60. J. Durst, C. Simon, F. Hasché, and H. A. Gasteiger, *Journal of Electrochem. Soc.*, **162**, F190 (2015).
61. D. van der Vliet, D. S. Strmcnik, C. Wang, V. R. Stamenkovic, N. M. Markovic, and M. T.-M. Koper, "On the importance of correcting for the uncompensated Ohmic resistance in model experiments of the oxygen reduction reaction." *J. Electroanal. Chem.*, **647**, 29 (2010).
62. S. S. Kocha, Y. Garsany, and D. Myers, "DOE webinar 'testing oxygen reduction reaction activity with the rotating disc electrode technique." (2013), accessed at 19/2/2024.
63. A. Stassi, I. Gatto, G. Monforte, V. Baglio, E. Passalacqua, V. Antonucci, and A. S. Aricò, *J. Power Sources*, **208**, 35 (2012).
64. H. Lohse-Busch, M. Duoba, K. Stutenberg, S. Iliev, M. Kern, B. Richards, M. Christenson, and A. Loiselle-Lapointe, "Technology Assessment of a Fuel Cell Vehicle: 2017 Toyota Mirai, Argonne National Laboratory Report ANL/ESD-18/12, page 37, Prepared for U.S. Department of Energy, Fuel Cell Technologies Office." June 2018, https://publications.anl.gov/anlpubs/2018/06/144774.pdf, accessed at 6/12/23.
65. J. P. Perdew, K. Burke, and M. Ernzerhof, "Generalized gradient approximation made simple." *Phys. Rev. Lett.*, **77**, 3865 (1996).
66. P. E. Blöchl, "Projector augmented-wave method." *Phys. Rev. B*, **50**, 17953 (1994).
67. G. Kresse and D. Joubert, "From ultrasoft pseudopotentials to the projector agumented-wave method." *Phys. Rev. B*, **59**, 1758 (1999).
68. G. Kresse and J. Hafner, "Ab initio molecular dynamics for open-shell transition metals." *Phys. Rev. B*, **48**, 13115 (1993).
69. G. Kresse and J. Furthmüller, "Efficient iterative schemes for ab initio total-energy calculations using plane-wave basis set." *Phys. Rev. B*, **54**, 11169 (1996).
70. M. J. Mehl, D. Hicks, C. Toher, O. Levy, R. M. Hanson, G. Hart, and S. Curtarolo, "The AFLOW library of crystallographic prototypes: part 1." *Comp. Mater. Sci.*, **136**, S1 (2017).
71. J. L.-F. Da Silva, C. Stampfl, and M. Scheffler, "Converged properties of clean metal surfaces by all-electron first-principles calculations." *Surf. Sci.*, **600**, 703 (2006).
72. P. Haas, F. Tran, and P. Blaha, "Calculation of the lattice constant of solids with semilocal functionals." *Phys. Rev. B*, **79**, 085104 (2009).
73. C. Kittel, *Introduction to Solid State Physics* 7th ed.(Wiley, New York) (1996).
74. K. Mathew, R. Sundararaman, K. Letchworth-Weaver, T. A. Arias, and R. G. Hennig, "Implicit solvation model for density-functional study of nanocrystal surfaces and reaction pathways." *J. Chem. Phys.*, **140**, 084106 (2014).
75. K. Mathew, V. S.-C. Kolluru, S. Mula, S. N. Steinmann, and R. G. Hennig, "Implicit self-consistent electrolyte model in plane-wave density-functional theory." *J. Chem. Phys.*, **151**, 234101 (2019).
76. G. Henkelman and H. Jónsson, "A climbing image nudged elastic band method for finding saddle points and minimum energy paths." *J. Chem. Phys.*, **113**, 9901 (2000).
77. G. Henkelman and H. Jónsson, "Improved tangent estimate in the nudged elastic band method for finding minimum energy paths and saddle points." *J. Chem. Phys.*, **113**, 9978 (2000).
78. W. Vielstich, *Cyclic voltammetry in Handbook of Fuel Cells - Fundamentals, Technology and Applications* (2003), 2, ed. W. Vielstich et al. (Wiley, Ltd.) p. 443.
79. N. Furuya and S. Koide, "Hydrogen adsorption on iridium single-crystal surfaces." *Surf. Sci.*, **226**, 221 (1990).
80. H. E. Hoster and H. A. Gasteiger, "Ex-situ surface preparation and analysis: Transfer between UHV and electrochemical cell in Handbook of Fuel Cells - Fundamentals." *Technology and Applications* (2003), 2, ed. W. Vielstich et al. (Wiley Ltd) p. 443.
81. T. J. Schmidt, H. A. Gasteiger, G. D. Stab, P. M. Urban, D. M. Kolb, and R. J. Behm, *J. Electrochem. Soc.*, **145**, 2354 (1998).
82. J. Perez, H. M. Villullas, and E. R. Gonzalez, *J. of Electroanalytical Chemistry*, **435**, 179 (1997).
83. Y. Lu, H. Zhang, Y. Wang, and Z. Chen, "First principles study on the oxygen reduction reaction of Ir@Pt core–shell structure." *Chem. Phys.*, **552**, 111356 (2022).
84. J. S. McEwen, J. M. Bray, C. Wu, and W. F. Schneider, "How low can you go? Minimum energy pathways for O_2 dissociation on Pt (111)." *Phys. Chem. Chem. Phys.*, **14**, 16677 (2012).
85. Y. Xu and M. Mavrikakis, "Adsorption and dissociation of O_2 on Ir (111)." *J. Chem. Phys.*, **116**, 10846 (2002).
86. D. Yang, B. Li, H. Zhang, and J. Ma, *Int. J. Hydrogen Energy*, **37**, 2447 (2012).
87. P. Urchaga, T. Kadyk, S. G. Rinaldo, A. O. Pistono, J. Hu, W. Lee, C. Richards, M. H. Eikerling, and C. A. Rice, "Catalyst degradation in fuel cell electrodes: accelerated stress tests and model-based analysis." *Electrochim. Acta*, **176**, 1500 (2015).